J. Fluid Mech. (2007), *vol.* 588, *pp.* 1–28.
doi:10.1017/S0022112007007410 Printed in the United Kingdom

Instability and focusing of internal tides in the deep ocean

OLIVER BÜHLER AND CAROLINE J. MULLER†

Center for Atmosphere Ocean Science at the Courant Institute of Mathematical Sciences, New York University, New York, NY 10012, USA

(Received 18 December 2006 and in revised form 7 April 2007)

The interaction of tidal currents with sea-floor topography results in the radiation of internal gravity waves into the ocean interior. These waves are called internal tides and their dissipation due to nonlinear wave breaking and concomitant three-dimensional turbulence could play an important role in the mixing of the abyssal ocean, and hence in controlling the large-scale ocean circulation.

As part of on-going work aimed at providing a theory for the vertical distribution of wave breaking over sea-floor topography, in this paper we investigate the instability of internal tides in a very simple linear model that helps us to relate the formation of unstable regions to simple features in the sea-floor topography. For two-dimensional tides over one-dimensional topography we find that the formation of overturning instabilities is closely linked to the singularities in the topography shape and that it is possible to have stable waves at the sea floor and unstable waves in the ocean interior above.

For three-dimensional tides over two-dimensional topography there is in addition an effect of geometric focusing of wave energy into localized regions of high wave amplitude, and we investigate this focusing effect in simple examples. Overall, we find that the distribution of unstable wave breaking regions can be highly non-uniform even for very simple idealized topography shapes.

1. Introduction

The topic of this paper is the generation of internal waves in the deep ocean through the interaction of barotropic tidal flow with sea-floor topography. This process is known as tidal conversion and the resulting internal waves are known as *internal tides*. Their generation, propagation, and eventual dissipation due to instability, wave breaking, and concomitant bursts of three-dimensional turbulence are currently believed to be important for the dynamics of the large-scale ocean circulation as a whole, especially in the deep, abyssal ocean below 1500 m depth or so (e.g. Munk & Wunsch 1998; Wunsch 2000; and the reviews in Wunsch & Ferrari 2004 and Thorpe 2005). These internal wave processes are far too small in spatial and/or temporal scale to be resolved in numerical ocean circulation models used for climate prediction, and therefore theory and observations must be used to parametrize their effects in such models.

To provide some background, it is known from astronomical observations that 3.5 terawatts (TW) are available from tidal forcing for eventual dissipation in the ocean

† Author to whom correspondence should be addressed.

(Egbert & Ray 2000, 2001). There is much less certainty about the distribution of this global dissipation, although there is reasonable agreement that approximately 2.5 TW of this dissipation occurs in shallow seas, such as the Irish sea, whereas the remaining 1 TW of dissipation occurs in the deep ocean and may involve the breaking of small-scale internal waves such as the internal tides. The turbulent mixing associated with these breaking waves makes a significant contribution to the diffusion of fluid particles across density surfaces, which is important for the maintenance of the stratification in the deep ocean (e.g. Wunsch & Ferrari 2004).

Egbert & Ray identify areas of the deep ocean where the barotropic tide seems to lose energy to the internal tides (Egbert & Ray 2000). These are areas of significant roughness, generally with elongated features such as ridges, trenches and island chains oriented perpendicular to tidal flows. These topographic features have slopes that vary over a wide range (Seibold & Berger 1996). Many oceanic islands and trenches are supercritical topographies, i.e. the local topography slope exceeds the propagation angle of the internal tides. An example is the Hawaiian Ridge, where a comprehensive observational program was recently conducted (e.g. Alford, Gregg & Merrifield 2006; Klymak *et al.* 2006; Lee *et al.* 2006; Aucan *et al.* 2006). On the other hand, large-scale features of mid-ocean ridge topographies such as the Mid-Atlantic Ridge are subcritical topographies. Observations of enhanced bottom mixing near the Mid-Atlantic Ridge was found during the Brazil Basin Tracer Release Experiment (Polzin *et al.* 1997; Ledwell *et al.* 2000).

Idealized analytical and numerical studies of tidal conversion have concentrated on the energy conversion rate, which is the rate at which internal-tide energy is produced by tidal conversion at the sea floor (e.g. Cox & Sandstrom 1962; Robinson 1969; Baines 1973; Bell 1975*a*, 1975*b*; Llewellyn Smith & Young 2002; Khatiwala 2003; St. Laurent & Garrett 2002; St. Laurent *et al.* 2003; Balmforth, Ierley & Young 2002; Llewellyn Smith & Young 2003; Di Lorenzo, Young & Llewellyn Smith 2006; Petrelis, Llewellyn Smith & Young 2006; Legg & Huijts 2006; see also Garrett & Kunze 2007 for a recent review). The analytical studies range from the simplest linear theory for infinitesimal sea-floor topography to more sophisticated techniques that allow for more accuracy in the kinematic boundary condition at the sea floor. The latter can also deal with supercritical topography. To date, the analytical studies of supercritical topography have been restricted to two-dimensional flows over one-dimensional topography. Somewhat surprisingly, these detailed investigations of tidal conversion on one-dimensional topography suggest that the simplest linear theory delivers results that are qualitatively reasonable and accurate in terms of energy conversion rate within a factor of two or so.

Large-scale numerical ocean circulation models used for climate prediction require a parametrization of small-scale mixing based on empirical maps of the global energy conversion rate at the sea floor together with *ad hoc* methods of how to distribute the energy dissipation and diffusivity due to breaking waves throughout the water column; see e.g. Ledwell *et al.* (2000), Egbert & Ray (2000), Jayne & Laurent (2001), Nycander (2005), and Hibiya, Nagasawa & Niwa (2006) for empirical data and St. Laurent, Simmons & Jayne (2002), Simmons *et al.* (2004), Saenko & Merryfield (2005), and Canuto *et al.* (2007) for parametrizations in numerical models. At present, there is little theory to guide these methods, in particular as far as the distribution of wave breaking in the vertical is concerned.

It is clear that a comprehensive understanding of internal tides and of their role in the ocean circulation must encompass an understanding of their generation, their instability, and also of their eventual breakdown into three-dimensional turbulence.

This paper aims at the instability part of this problem, i.e. we consider in detail the formation of unstable flow regions in the wave field and how this relates to the shape of the sea-floor topography. We interpret these instability regions as the seeds of the three-dimensional turbulence that ultimately produces the small-scale mixing that is relevant to the ocean circulation. Of particular interest for us are wave fields that show no obvious signs of instability in broad measures such as the root-mean-square value of the Richardson number. Such wave fields are nevertheless capable of forming localized pockets of instability, especially in three-dimensional flow where there is the possibility for geometric focusing of wave energy. Geometric focusing is a genuinely three-dimensional flow phenomenon, i.e. it does not occur in the most commonly studied case of two-dimensional flow over one-dimensional topography.

We use the simplest form of linear theory in this paper. This is motivated by convenience and by the previously noted observation that more sophisticated theories predict surprisingly similar results. In other words we consider gentle widespread subcritical topographies such as features of the Mid-Atlantic Ridge. We concentrate on a real-space representation of the internal tides using Green's functions rather than on the more usual spectral representation using Fourier modes. This is because we want to investigate in detail the formation of high-amplitude regions in the real-space wave field, and for this aim the Fourier representation is not very helpful.

We present results for both two-dimensional and three-dimensional flows over idealized sea-floor topography. The two-dimensional results are not essential for the practical application but they serve to introduce the main ideas and techniques in preparation for the three-dimensional results. Our main aim is to obtain a clear understanding of where the linear wave field is unstable and of how this can be related to topography features such as localized singularities or more extended features that may lead to focusing in the ocean interior. A particular and recurring question will be to understand under what conditions instability in the ocean interior occurs without there being instability directly at the topography. This question has clear implications for the distribution of the wave breaking regions throughout the water column. We plan to follow up on this question in future work.

The paper is laid out as follows. In § 2 we study internal tides due to two-dimensional flow over one-dimensional topography, which admits a very simple representation using a Green's function; this highlights the importance of singularities in the topography shape in this case. In § 3 the case of two-dimensional topography is studied, which has a more complicated Green's function that, however, is amenable to a simple far-field expansion along characteristic surfaces. This produces a simple geometric theory of internal tides away from the boundary and leads us to the focusing effect, which is then discussed in detail in § 4. Concluding remarks are offered in § 5.

Finally, we would like to point out in passing that this study is not based on ray tracing, i.e. we do not assume a slowly varying wavetrain. Time-periodic internal waves are peculiar because their spatial structure is governed by a hyperbolic equation (e.g. (2.6) below; Sobolev 1960; Maas & Lam 1995) whose characteristics indeed coincide with the usual group-velocity rays; this can be confusing at times.

2. Internal tides in two dimensions

Our goal is to study linear waves generated by the flow of a uniformly stratified fluid with barotropic tidal velocity $\boldsymbol{U}(t)$ over undulating sea-floor topography. Specifically, let (x, y) denote the horizontal coordinates, z the vertical coordinate, and let the

x-axis be aligned with the tidal velocity $\boldsymbol{U}(t) = (U_0 \cos \omega_0 t, 0, 0)$ where $\omega_0 > 0$ denotes the tidal frequency. Without bottom topography this barotropic tide represents the basic solution to the usual tidal equations, and we consider a linear perturbation to this solution caused by infinitesimal sea-floor topography $z = h(x, y)$ relative to the unperturbed sea floor $z = 0$. The perturbed flow takes the form of internal tides, which are the internal waves that are generated by the sloshing of the barotropic tide over the undulating topography. We consider a linear Boussinesq model with constant buoyancy frequency N and Coriolis parameter f and infinite vertical extent. For simplicity, this omits all effects to do with variable stratification and finite ocean depth, in particular it omits wave reflection in the vertical.

Even with these simplifications the linear problem for internal tides forced by sinusoidal topography $h = h_0 \cos(kx)$ with wavenumber k is known to be hard (e.g. Baines 1973). In general, subtle Doppler-shifting effects lead to the generation of waves not just at frequency $\omega_0 > 0$ but at higher harmonics of ω_0 as well. More specifically, the intrinsic frequency spectrum of the waves can be seen to be given by the frequency spectrum of the vertical motion of a fluid particle that follows the tidal sloshing across the topography. This spectrum is therefore critically dependent on the non-dimensional tidal excursion parameter $U_0/L\omega_0$, which measures the horizontal tidal excursions of size U_0/ω_0 against the gradient length scale of the topography $L = 1/k$.

Simple solutions are available if this parameter is either large or small. For instance, in the limit $\omega_0 \to 0$ the excursion parameter is large and the spectrum concentrates at the Doppler-shifting frequency $U_0 k$; this is the usual lee-wave regime. Conversely, for small values of the excursion parameter the spectrum concentrates on the tidal frequency ω_0 itself, i.e. Doppler-shifting effects are unimportant in this regime. It follows that $U\partial/\partial x \ll \partial/\partial t$ and advection by the tides can be neglected. In other words, the problem reduces to the forcing of a quiescent body of fluid by oscillatory vertical motion at its lower boundary. This is the regime we will study here and therefore we assume

$$\frac{U_0 k}{\omega_0} = \frac{U_0}{\omega_0 L} \ll 1. \tag{2.1}$$

Of course, this assumption limits the maximum horizontal wavenumber of the topography. However, with $U_0 = 3\,\mathrm{cm\,s^{-1}}$ and $\omega_0 = 1.4 \times 10^{-4}\,\mathrm{s^{-1}}$ for the semi-diurnal tide (see Bell 1975*b*), the tidal excursion is only 215 m, which is smaller than most topographic features of interest.

In this section we consider the two-dimensional problem in the xz-plane such that $\partial/\partial y = 0$ for all fields including the bottom topography $h(x)$. In § 3 we will return to the three-dimensional problem with full $h(x, y)$. The governing equations are the linear Boussinesq equations in standard notation:

$$\left.\begin{aligned} \frac{\partial u}{\partial t} - fv + \frac{1}{\rho_0}\frac{\partial p}{\partial x} = 0, \quad \frac{\partial v}{\partial t} + fu = 0, \\ \frac{\partial w}{\partial t} + \frac{1}{\rho_0}\frac{\partial p}{\partial z} = b, \quad \frac{\partial b}{\partial t} + N^2 w = 0, \\ \frac{\partial u}{\partial x} + \frac{\partial w}{\partial z} = 0. \end{aligned}\right\} \tag{2.2}$$

There are no terms such as $U\partial u/\partial x$ etc., because of (2.1). Here $b = -g(\rho - \rho_s(z))/\rho_0$ is the usual buoyancy disturbance given in terms of gravity g, density ρ, constant reference density ρ_0, and the linear background stratification $\rho_s(z) = \rho_0(1 - N^2 z/g)$.

The flow is forced by the kinematic boundary condition $w = U(t)\partial h/\partial x$ at the lower boundary $z = 0$. We also impose a radiation condition, i.e. the energy carried by the waves radiates away from the topography. We note in passing that this system also applies to one-dimensional topography at an arbitrary angle to the tidal velocity because adding a y-component to the tidal velocity would not change the above equations or the boundary condition and therefore the same wave field would be generated.

2.1. *Solution in Fourier space*

The above system of equations can be reduced to a single equation for the stream-function ψ such that $(u, w) = (-\psi_z, \psi_x)$, namely

$$\left(f^2 + \frac{\partial^2}{\partial t^2}\right)\frac{\partial^2 \psi}{\partial z^2} + \left(N^2 + \frac{\partial^2}{\partial t^2}\right)\frac{\partial^2 \psi}{\partial x^2} = 0. \tag{2.3}$$

The general solution consists of plane waves with frequency ω_0 and xz-wavenumbers (k, m). From the dispersion relation we have

$$\mu = \left|\frac{m}{k}\right| = \sqrt{\frac{N^2 - \omega_0^2}{\omega_0^2 - f^2}} \tag{2.4}$$

and the slope of the group-velocity rays is $\mathrm{d}z/\mathrm{d}x = \pm\mu^{-1}$. Typically in the deep ocean μ takes moderate values of order unity. For instance, with the representative near-bottom buoyancy frequency $N = 5f - 10f$ and $f = \omega_0/2$ at a latitude of 30°, $\mu = 2.6 - 5.7$, and therefore the slope $\mathrm{d}z/\mathrm{d}x = \mu^{-1}$ is about a quarter or so. In the upper ocean N is about ten times bigger and the slope flattens correspondingly.

It is convenient to define the scaled vertical coordinate $Z = \mu z$ and the non-dimensionalized topography $H(x)$ by $h(x) = h_0 H(x)$. Following Balmforth *et al.* (2002) we look for solutions of the form

$$\psi(x, z, t) = U_0 h_0 \mathrm{Re}(\phi(x, Z)\mathrm{e}^{-\mathrm{i}\omega_0 t}), \tag{2.5}$$

and (2.3) becomes a one-dimensional wave equation where Z plays the role of time

$$\frac{\partial^2 \phi}{\partial Z^2} - \frac{\partial^2 \phi}{\partial x^2} = 0 \tag{2.6}$$

with lower boundary condition

$$\phi(x, Z = 0) = H(x). \tag{2.7}$$

However, the radiation condition means that this is not the standard Cauchy problem for the wave equation. The radiation condition necessitates the use of Fourier transforms at this stage.

From now on, we assume that $H(x)$ is a function on the real line that decays to zero as $|x| \to \infty$. In other words, we are interested in isolated topography. Of course, the periodic case can be studied by the same method with Fourier series replacing transforms. Consider the Fourier transform of ϕ in x:

$$\hat{\phi}(k, Z) = FT\{\phi\}(k, Z) = \int_{-\infty}^{\infty} \phi(x, Z)\mathrm{e}^{-\mathrm{i}kx}\,\mathrm{d}x, \tag{2.8}$$

$$\phi(x, Z) = FT^{-1}\{\hat{\phi}\}(x, Z) = \frac{1}{2\pi}\int_{-\infty}^{\infty} \hat{\phi}(k, Z)\mathrm{e}^{\mathrm{i}kx}\,\mathrm{d}k. \tag{2.9}$$

Then (2.6) yields $m = \pm k$. For internal waves, the vertical group and phase velocities have opposite signs and therefore the radiation condition implies negative vertical

phase velocity, i.e. $m\omega_0 < 0$. Imposing the radiation condition for $\psi(x, z, t)$ on each mode along with (2.7) and with the convention $\omega_0 > 0$ we obtain $m = -|k|$, and therefore

$$\hat{\phi}(k, Z) = \hat{H}(k)\mathrm{e}^{-\mathrm{i}|k|Z}. \tag{2.10}$$

This is the solution in Fourier space. Note that this is not the Fourier transform of a real function for $Z > 0$. Indeed, its real part will contribute to the wave field with a $\cos\omega_0 t$ factor and its imaginary part with a $\sin\omega_0 t$ factor.

The time-averaged energy conversion rate C quantifies the mean energy flux of the internal tides, which presumably is ultimately related to the deep-ocean mixing caused by dissipating or breaking internal tides. The conversion rate is quadratic in wave amplitude and additive over all Fourier components because of orthogonality. This means that it can be computed directly from the solution in Fourier space. Indeed, the conversion rate of energy per unit length in y is simply the time average, denoted by brackets, of the vertical flux of energy at $Z = 0$:

$$C = \left\langle \int_{-\infty}^{\infty} p(x, 0, t)w(x, 0, t)\,\mathrm{d}x \right\rangle = \left\langle \frac{1}{2\pi}\int_{-\infty}^{\infty} \hat{p}(k, 0, t)\hat{w}^*(k, 0, t)\,\mathrm{d}k \right\rangle \tag{2.11}$$

by Parseval's theorem, where $\hat{w}^*$ denotes the complex conjugate of $\hat{w}$. From (2.2) and (2.10),

$$\hat{w}(k, 0, t) = U_0 h_0 FT\left\{H'(x)\right\}\cos(\omega_0 t), \tag{2.12}$$

$$\hat{p}(k, 0, t) = \frac{\rho_0 U_0 h_0}{\omega_0}\sqrt{N^2 - \omega_0^2}\sqrt{\omega_0^2 - f^2}\,\frac{1}{|k|}FT\left\{H'(x)\right\}\cos(\omega_0 t), \tag{2.13}$$

where the prime denotes x-differentiation. Therefore

$$C = C_0\int_{-\infty}^{\infty}|k|\left|\hat{H}(k)\right|^2\mathrm{d}k,\ C_0 = \frac{1}{4\pi}\frac{\rho_0 U_0^2 h_0^2}{\omega_0}\sqrt{N^2 - \omega_0^2}\sqrt{\omega_0^2 - f^2}. \tag{2.14}$$

We recover Bell's formula (Bell 1975*a*) for the contribution of the waves with tidal frequency ω_0 to the conversion rate in the limit $N/\omega_0 \gg 1$; see, for instance, equation (2) in Llewellyn Smith & Young (2002), who extended Bell's formula to non-zero f.

The energy conversion rate has an interesting dependence on the shape of the topography described by the integral in (2.14).† This can be brought out by considering the family of stretched and scaled topographies defined by $H_\delta^p(x) \equiv \delta^p H(x/\delta)$ where $\delta > 0$ and p is a real number. Thus, $H_1^1(x) = H(x)$, the Fourier transform of H_δ^p is $\hat{H}_\delta^p(k) = \delta^{p+1}\hat{H}(k\delta)$, and we obtain

$$\begin{aligned} C_\delta^p &= C_0\int_{-\infty}^{\infty}|k|\left|\hat{H}_\delta^p(k)\right|^2\mathrm{d}k = C_0\int_{-\infty}^{\infty}|k|\delta^{2p+2}\left|\hat{H}(k\delta)\right|^2\mathrm{d}k \\ &= C_0\delta^{2p}\int_{-\infty}^{\infty}|\delta k|\left|\hat{H}(\delta k)\right|^2\mathrm{d}\delta k = \delta^{2p}C_1^1. \end{aligned} \tag{2.15}$$

This shows the surprising result that the conversion rate is invariant if $p = 0$, i.e. the conversion rate is unaffected by any pure stretching transformation $H(x) \to H(x/\delta)$. Llewellyn Smith & Young (2002) point out this invariance in the case of the witch of Agnesi, but (2.15) makes obvious that this invariance in fact holds for any compact topography shape.

† The same integral appears in the computation of the form drag due to hydrostatic lee waves.

Physically, this invariance is due to the cancellation of two counter-acting effects, as can be seen in the case of a localized topographic wave packet with width W and central wavenumber k, say. Compressing the wavepacket with $\delta < 1$ increases the central wavenumber by a factor $1/\delta$, which increases the conversion rate per unit width of the packet according to the k-weighting in (2.14) by the same factor $1/\delta$. On the other hand, the width W is reduced by a factor δ and this precisely cancels the first effect.‡

2.2. *Solution using Green's function*

The solution in terms of inverse Fourier transforms is convenient for computation of the conversion rate, which was a single number, but it is not convenient in order to investigate the behaviour of the solution, say, as a function of distance above the topography. However, the latter is necessary in order to study local instabilsities of the wave field. For this purpose it is more convenient to have a real-space representation of the solution in terms of a Green's function. In fact, in the present two-dimensional case this leads to a very simple representation of the solution in terms of the topography shape and its Hilbert transform. We believe that this is well known, but the approach is summarized here as preparation for the less simple three-dimensional case.

From (2.10) the streamfunction is obtained from the topography by the x-convolution

$$\phi(x, Z) = (G * H)(x) = \int_{-\infty}^{\infty} G(x - x', Z) H(x')\, \mathrm{d}x', \tag{2.16}$$

where $G(x, Z) \equiv FT^{-1}\{\mathrm{e}^{-\mathrm{i}|k|Z}\}$ is the causal Green's function. This is a distribution, which can be computed explicitly (see Appendix A) as

$$G(x, Z) = \frac{1}{2}(\delta(x + Z) + \delta(x - Z)) + \frac{\mathrm{i}}{2\pi}\left(\frac{1}{x - Z} - \frac{1}{x + Z}\right). \tag{2.17}$$

The streamfunction is therefore given by

$$\phi = G * H = \frac{1}{2}\,(H(x + Z) + H(x - Z)) + \frac{\mathrm{i}}{2\pi}\int \left(\frac{H(x')}{x - Z - x'} - \frac{H(x')}{x + Z - x'}\right) \mathrm{d}x' \tag{2.18}$$

with the integral defined by its Cauchy principal value; this is the Hilbert transform of H. Specifically, if we denote the Hilbert transform of a function f by $\tilde{f} \equiv 1/\pi x * f$ then we can rewrite (2.18) as

$$\phi = G * H = \frac{1}{2}[H(x + Z) + H(x - Z)] + \frac{\mathrm{i}}{2}[\tilde{H}(x - Z) - \tilde{H}(x + Z)]. \tag{2.19}$$

This surprisingly simple expression demonstrates that ϕ is a linear combination of shifted values of the topography H and its Hilbert transform $\tilde{H}$ along the characteristics $\mathrm{d}Z = \mathrm{d}x$ and $\mathrm{d}Z = -\mathrm{d}x$ of the hyperbolic equation (2.6). From (2.5) the time-dependent streamfunction is given by

$$\psi(x, z, t) = \frac{U_0 h_0}{2}\left\{\cos\omega_0 t\,[H(x + Z) + H(x - Z)] + \sin\omega_0 t\,[\tilde{H}(x - Z) - \tilde{H}(x + Z)]\right\},$$

‡ For periodic topography stretching is permitted if $\delta = 1/n$ with integer n, but in this case the second effect is absent and the conversion rate per period length would indeed be proportional to n.

which illustrates that the real and imaginary parts of ϕ correspond to in-phase and out-of-phase oscillations relative to the tidal velocity $U(t) = U_0 \cos \omega_0 t$.

In general, for any function of the linear wave field, an x-convolution with the Green's function $G(x, Z)$ provides a map between the function at the lower boundary $Z = 0$ and the function at $Z \geqslant 0$, i.e.

$$A(x, Z) = G(x, Z) * A(x, 0) \Leftrightarrow \hat{A}(k, Z) = \exp(-\mathrm{i}|k|Z)\, \hat{A}(k, 0) \tag{2.20}$$

holds for any complex wave field A defined in analogy with ϕ in (2.5). The explicit action of $G(x, Z)$ on $A(x, 0)$ can be read off from (2.19). In fact, there is nothing special about the location $Z = 0$ because (2.20b) makes it obvious that G satisfies the group property $G(x, Z_1 + Z_2) = G(x, Z_1) * G(x, Z_2)$ for arbitrary Z_1 and Z_2. Thus we can view G as the unique linear operator that maps wave fields between different altitudes. In other words, G is the propagator of the wave field in altitude Z.

2.3. *Instabilities of the wave field*

We now investigate the possible instability of the internal tide solution. More specifically, we are looking for strong, fast, and catastrophic instabilities that signal the inevitable breakdown of linear theory and thereby mark the incipient stage of localized three-dimensional turbulence and therefore of irreversible mixing. In other words, we are using linear theory to predict its own breakdown. For simplicity, this omits all weaker nonlinear interaction effects such as resonant triad interactions, which could be viewed as weak instabilities of the linear wave field that operate over long, amplitude-dependent time scales and tend to preserve the energy of the wave field.

Thus, we use a simple measure of wave amplitude based either on Kelvin–Helmholtz instability flagged by low Richardson number or based on convective instability flagged by negative stratification. With Coriolis forces and three-dimensional flows it is simpler to look at the latter, and therefore we look at the stratification surfaces of constant $\Theta = b + N^2 z = b + N^2 Z/\mu$, which is proportional to the materially conserved density in the Boussinesq model for the ocean. Negative stratification corresponds to overturning of the stratification surfaces such that $\partial\Theta/\partial Z$ is negative. From (2.2) we find

$$\frac{\partial \Theta}{\partial Z} = \frac{N^2}{\mu}\left\{1 - \frac{U_0 h_0 \mu}{\omega_0}\frac{\partial}{\partial Z}\mathrm{Re}\left[\mathrm{i}\mathrm{e}^{-\mathrm{i}\omega_0 t}\frac{\partial \phi}{\partial x}\right]\right\} = \frac{N^2}{\mu}\{1 - \mathrm{Re}[\mathrm{e}^{-\mathrm{i}\omega_0 t} A(x, Z)]\}. \tag{2.21}$$

This introduces the non-dimensional wave amplitude

$$A(x, Z) \equiv \mathrm{i}\frac{U_0 h_0 \mu}{\omega_0}\frac{\partial}{\partial Z}\frac{\partial \phi}{\partial x} = A_r(x, Z) + \mathrm{i}A_i(x, Z) \tag{2.22}$$

such that

$$\frac{\partial \Theta}{\partial Z} = \frac{N^2}{\mu}\{1 - [\cos \omega_0 t\, A_r(x, Z) + \sin \omega_0 t\, A_i(x, Z)]\} \tag{2.23}$$

and $|A| \geqslant 1$ signals convective instability at some point in the oscillation. Combining (2.22) and (2.19) yields

$$A_r = \frac{1}{2}\frac{U_0 h_0 \mu}{\omega_0}[\tilde{H}''(x+Z) + \tilde{H}''(x-Z)], \quad A_i = \frac{1}{2}\frac{U_0 h_0 \mu}{\omega_0}[H''(x+Z) - H''(x-Z)] \tag{2.24}$$

where prime denotes differentiation. We observe that the wave amplitude is proportional to the second derivative of the topography and of its Hilbert transform.

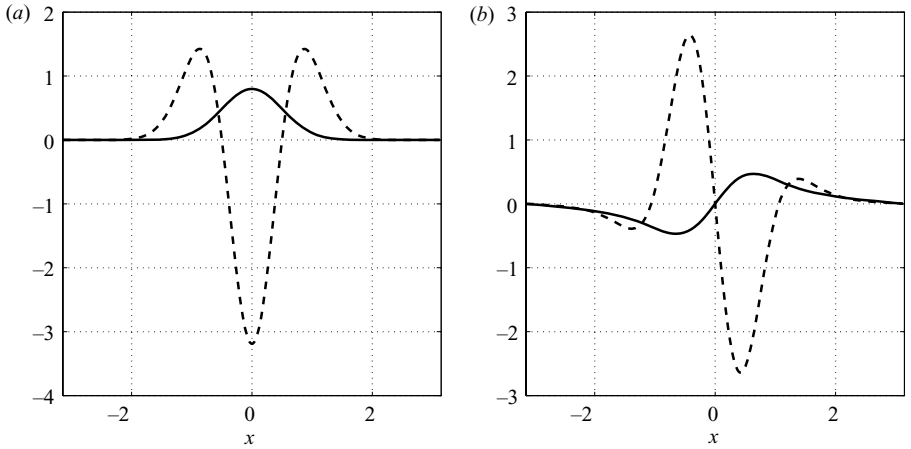

FIGURE 1. (*a*) A Gaussian bump $H(x) = \exp(-x^2/2\sigma^2)/(\sqrt{2\pi}\sigma)$ with $\sigma = 0.5$ and its second derivative (plain and dashed line, respectively), along with (*b*) their Hilbert transforms $\tilde{H}$ and $\tilde{H}''$ (plain and dashed line, respectively). By (2.24), the dashed line in (*b*) is proportional to the amplitude of the wave field at $Z = 0$.

Also, the term involving the Hilbert transform $\tilde{H}''$ is in phase with the tidal velocity $U(t)$, whilst the term involving H'' is ninety degrees out of phase.

It is useful to consider separately the wave amplitude field at the lower boundary $Z = 0$ and the propagated amplitude field in the ocean interior $Z > 0$. At $Z = 0$, the wave amplitude is $A_0(x) = A(x, 0) = A_r(x, 0) = (U_0 h_0 \mu/\omega_0)\tilde{H}''(x)$ such that

$$Z = 0: \quad \frac{\partial \Theta}{\partial Z} = \frac{N^2}{\mu}\left\{1 - \frac{U_0 h_0 \mu}{\omega_0}\cos\omega_0 t\ \tilde{H}''(x)\right\}. \tag{2.25}$$

We observe that at the lower boundary the wave amplitude does not depend on $H(x)$, is in phase with the tidal velocity, and hence there will be overturning instabilities when and where $\cos(\omega_0 t)\tilde{H}''(x) > \omega_0/U_0 h_0 \mu$. To illustrate this let us look at the smooth single-bump topography in figure 1. The boundary amplitude A_0 has a positive maximum before the bump and a negative minimum after the bump. Hence $\cos\omega_0 t\, A_0(x)$ is maximum at $\omega_0 t = 0$ on the left of the topography, and at $\omega_0 t = \pi$ on the right of the topography. In either case, $\cos\omega_0 t\, A_0(x)$ assumes its maximum value on the current upwind side relative to the oscillating tidal flow $U_0 \cos\omega_0 t$.

By (2.20), at any depth $Z \geqslant 0$ the amplitude of the wave field is given by $A(x, Z) = G(x, Z) * A_0(x)$, which is (2.24). The amplitude in the interior depends on both $H(x)$ and $\tilde{H}$ and instabilities will again occur when and where

$$\cos\omega_0 t[\tilde{H}''(x+Z) + \tilde{H}''(x-Z)] + \sin\omega_0 t[H''(x+Z) - H''(x-Z)] > 2\frac{\omega_0}{U_0 h_0 \mu}. \tag{2.26}$$

This makes clear that it is possible for the wave amplitude at the sea floor to be very different from the wave amplitude in the ocean interior simply because $A(x, 0)$ depends on $\tilde{H}''$ only, whereas $A(x, Z)$ depends on both $\tilde{H}''$ and H''. As is well known, the smallness of a function does not imply the smallness of its Hilbert transform, or *vice versa*. A simple example of this is a bounded discontinuous function like a step function, the Hilbert transform of which exhibits a logarithmic singularity at the jump location.

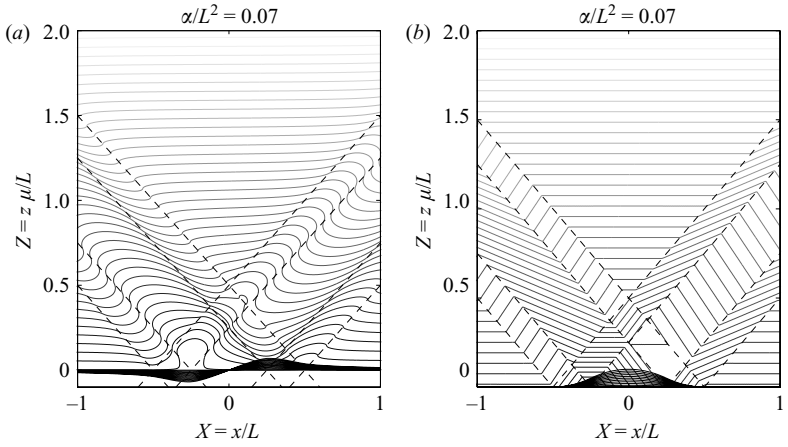

FIGURE 2. Buoyancy surfaces at $\omega_0 t = 0$ (a) and $\omega_0 t = \pi/2$ (b) when H'' has discontinuities. The parameter $\alpha = U_0 h_0 \mu/\omega_0$.The dashed lines are the characteristic lines emanating from discontinuities of H''. At the bottom, $0.1\tilde{H}(X)$ and $0.1H(X)$ are shown in (a) and (b) respectively (the scaling factor 0.1 has been introduced for better visualization of the wave field). Note that on the characteristics that do not intersect the support of H, the buoyancy surfaces are undisturbed at $\omega_0 t = \pi/2$. This is not true at $\omega_0 t = 0$, since the Hilbert transform involves a non-local convolution and hence $\tilde{H}''$ does not have compact support.

This is illustrated in figure 2, which depicts the internal tide due to topography with piecewise constant H'', in other words H is piecewise quadratic. Specifically, H is given by

$$H(X) = 8\left(X + \tfrac{1}{2}\right)^2 \chi_{[-1/2,-1/4]} + 8\left(\tfrac{1}{8} - X^2\right) \chi_{[-1/4,1/4]} + 8\left(X - \tfrac{1}{2}\right)^2 \chi_{[1/4,1/2]}. \quad (2.27)$$

where $X = x/L$ and χ denotes the indicator function. The corresponding H'' has discontinuities at $\pm 1/2$ and $\pm 1/4$ and hence its Hilbert transform is unbounded along the characteristics emanating from these locations. We expect overturning to occur near these characteristics when $\cos(\omega_0 t) = 1$ and this is illustrated in figure 2. Away from these singular characteristics the stratification surfaces undulate with a typical slope $U_0 h_0 \mu/(\omega_0 L^2)$. In terms of physical numbers, for a ridge with height $h_0 = 400\,\mathrm{m}$ and width $L = 10\,\mathrm{km}$, and using semi-diurnal values $U_0 = 4 \times 10^{-2}\,\mathrm{m\,s^{-1}}$, $f_0 = 10^{-4}\,\mathrm{s^{-1}}$, $N = 10 f_0$ and $\omega_0 = 2 f_0$, we obtain $U_0 h_0 \mu/(\omega_0 L^2) \approx 4 \times 10^{-3}$. Nonetheless, in order to display the wave field clearly, we used the rather large value $U_0 h_0 \mu/(\omega_0 L^2) = 7 \times 10^{-2}$ in figure 2.

The presence of overturning is a robust result for the first mode (at fundamental tidal frequency ω_0) even for finite tidal excursion $U_0/L\omega_0$. If we remove the small tidal excursion assumption (2.1) but retain discontinuous H'', then there can still be overturning but the amplitude is now bounded with a logarithmic singularity in the tidal excursion parameter (see Appendix B for solutions in the finite tidal excursion regime).

It is worth noting that the presence of flow instabilities and wave breaking entirely due to isolated jumps in H'' is probably not associated with a large dissipation of energy. This is because any isolated discontinuity in H'' could be smoothed out by convolution with a suitable mollifier (see, for instance, Appendix C4 in Evans 1998). This would reduce or even suppress the overturning without necessarily significantly modifying the energy conversion rate, which by (2.14) is proportional to the integral

of $k|\hat{H}|^2$ over positive k. A jump in H'' leads to $|\hat{H}| \propto k^{-3}$ as $k \to \infty$, and therefore the integrand has the rapid decay rate k^{-5}. Smoothing the singularity of H'' suppresses this power law tail, but this would have little impact on the net energy conversion rate.

Finally, it is remarkable how the wave structure in this case of small tidal excursion differs from that of lee waves, which illustrate the opposite case of infinite excursion as a steady wind $U > 0$ blows over isolated topography. For instance, for hydrostatic wavenumbers $U^2k^2 \ll N^2$ with $f = 0$ the vertical wavenumber for lee waves is simply $m = \mathrm{sgn}(k)N/U$, which does not depend on the horizontal wavelength. In this case $\partial\Theta/\partial z = N^2\{1 - A(x, z)\}$, and the corresponding overturning amplitude for steady lee waves is found to be

$$A(x, Z) = -\frac{Nh_0}{U}(\tilde{H}(x)\cos Z + H(x)\sin Z) \tag{2.28}$$

where $Z = zN/U$. Broadly, this shows that lee waves are localized over the topography and that their amplitude is proportional to H and $\tilde{H}$. This is very different from the waves in figure 2, which spread out with amplitudes proportional to H'' and $\tilde{H}''$.

3. Internal tides in three dimensions

We now come to the main topic of the paper, which is the study of three-dimensional internal tides. *Mutatis mutandis*, the solution in Fourier modes and the Green's function are derived as in the two-dimensional case. However, there is now a fundamentally new phenomenon that did not appear in the two-dimensional case, namely the geometrical focusing of wave energy into point- or line-like regions of the ocean interior. This important phenomenon can lead to increased amplitudes in these focusing regions, which are hence prime locations for wave breaking. We will briefly summarize the Fourier and Green's function solution in this section and thereafter we will look in depth at the focusing phenomenon in § 4.

We again consider barotropic tidal flow $\boldsymbol{U}(t) = (U_0\cos\omega_0 t, 0, 0)$ above topography $h(x, y) = h_0H(x, y)$. The assumptions are the same as in the two-dimensional case (in particular, weak topography approximation and small tidal excursion limit) except that we no longer assume $\partial/\partial y = 0$. With the same notation as in § 2, the equations become

$$\left.\begin{aligned} \frac{\partial u}{\partial t} - fv + \frac{1}{\rho_0}\frac{\partial p}{\partial x} = 0,\ \frac{\partial v}{\partial t} + fu + \frac{1}{\rho_0}\frac{\partial p}{\partial y} = 0, \\ \frac{\partial w}{\partial t} + \frac{1}{\rho_0}\frac{\partial p}{\partial z} = b,\ \frac{\partial b}{\partial t} + N^2 w = 0, \\ \frac{\partial u}{\partial x} + \frac{\partial v}{\partial y} + \frac{\partial w}{\partial z} = 0, \end{aligned}\right\} \tag{3.1}$$

with the linearized boundary condition $w = U_0\cos(\omega_0 t)\partial h/\partial x = h_0U_0\cos(\omega_0 t)\partial H/\partial x$ at $z = 0$. We also impose the upward radiation condition as before.

For internal waves, the above system of equations can be reduced to a single equation for the vertical velocity

$$\left(f^2 + \frac{\partial^2}{\partial t^2}\right)\frac{\partial^2 w}{\partial z^2} + \left(N^2 + \frac{\partial^2}{\partial t^2}\right)\nabla_H^2 w = 0 \tag{3.2}$$

where ∇_H^2 is the horizontal Laplacian $\partial^2/\partial x^2 + \partial^2/\partial y^2$.

3.1. *Solution in Fourier space*

We take $Z = \mu z$ as before and look for a solution of the form

$$w(x, y, z, t) = U_0 h_0 \mathrm{Re}(W(x, y, Z)\mathrm{e}^{-\mathrm{i}\omega_0 t}). \tag{3.3}$$

Then (3.2) becomes

$$\frac{\partial^2 W}{\partial Z^2} - \nabla_H^2 W = 0. \tag{3.4}$$

As in the two-dimensional case, we now assume that $H(\boldsymbol{x})$ is compactly supported, i.e. we are interested in isolated topographic features. Consider the Fourier transform of W over $\boldsymbol{x} = (x, y)$

$$\hat{W}(\boldsymbol{k}, Z) = FT\{W\}(\boldsymbol{k}, Z) = \int_{-\infty}^{\infty}\int_{-\infty}^{\infty} W(\boldsymbol{x}, Z)\mathrm{e}^{-\mathrm{i}\boldsymbol{k}\cdot\boldsymbol{x}}\,\mathrm{d}x\,\mathrm{d}y, \tag{3.5}$$

$$W(\boldsymbol{x}, Z) = FT^{-1}\{\hat{W}\}(\boldsymbol{x}, Z) = \frac{1}{(2\pi)^2}\int_{-\infty}^{\infty}\int_{-\infty}^{\infty} \hat{W}(\boldsymbol{k}, Z)\mathrm{e}^{\mathrm{i}\boldsymbol{k}\cdot\boldsymbol{x}}\,\mathrm{d}k\,\mathrm{d}l. \tag{3.6}$$

Here the wavenumber vector is $\boldsymbol{k} = (k, l)$. Imposing the radiation condition on each mode along with the bottom boundary condition $W(\boldsymbol{x}, 0) = \partial H(\boldsymbol{x})/\partial x$, we obtain

$$\hat{W}(\boldsymbol{k}, Z) = \exp(-\mathrm{i}|\boldsymbol{k}|Z)\, FT\left\{\frac{\partial H}{\partial x}\right\} = \exp(-\mathrm{i}|\boldsymbol{k}|Z)\,\mathrm{i}k\hat{H}(\boldsymbol{k}). \tag{3.7}$$

Note that as in the two-dimensional case, this is not the Fourier transform of a real function for $Z > 0$. Its real part contributes to the wave field with a $\cos\omega_0 t$ factor in phase with the tide, and its imaginary part contributes with a $\sin\omega_0 t$ factor out of phase with the tide.

Again, the conversion rate of energy from the barotropic tide to the waves is the time average, denoted by brackets, of the vertical flux of energy at $Z = 0$,

$$C = \left\langle \int_{-\infty}^{\infty}\int_{-\infty}^{\infty} p(\boldsymbol{x}, 0, t)w(\boldsymbol{x}, 0, t)\,\mathrm{d}x\,\mathrm{d}y \right\rangle = \left\langle \frac{1}{(2\pi)^2}\int_{-\infty}^{\infty}\int_{-\infty}^{\infty} \hat{p}(\boldsymbol{k}, 0, t)\hat{w}^*(\boldsymbol{k}, 0, t)\,\mathrm{d}k\,\mathrm{d}l \right\rangle \tag{3.8}$$

by Parseval's theorem. Denoting $\kappa = |\boldsymbol{k}| = \sqrt{k^2 + l^2}$, it follows from (3.1) and (3.7) that

$$\hat{w}(\boldsymbol{k}, 0, t) = U_0 h_0 FT\left\{\frac{\partial H}{\partial x}\right\}\cos(\omega_0 t), \tag{3.9}$$

$$\hat{p}(\boldsymbol{k}, 0, t) = \frac{\rho_0 U_0 h_0}{\omega_0}\sqrt{N^2 - \omega_0^2}\sqrt{\omega_0^2 - f^2}\,\frac{1}{\kappa}FT\left\{\frac{\partial H}{\partial x}\right\}\cos(\omega_0 t). \tag{3.10}$$

Therefore

$$C = C_0\int_{-\infty}^{\infty}\int_{-\infty}^{\infty}\frac{k^2}{\kappa}\left|\hat{H}(\boldsymbol{k})\right|^2\,\mathrm{d}k\,\mathrm{d}l, \quad C_0 = \frac{1}{2(2\pi)^2}\frac{\rho_0 U_0^2 h_0^2}{\omega_0}\sqrt{N^2 - \omega_0^2}\sqrt{\omega_0^2 - f^2}. \tag{3.11}$$

In the limit $N/\omega_0 \gg 1$, we recover formula (54) from Llewellyn Smith & Young (2002) for an ocean of infinite depth and with $V_0 = 0$.

Let us compute the conversion rates for a family of simultaneously stretched and scaled topographies $H_\delta^p(\boldsymbol{x}) = \delta^p H(\boldsymbol{x}/\delta)$, where $\delta > 0$ and p is a real number. If the original topography H has its support included in some disk of radius L, then H_δ^p has support within a disk of radius δL. The Fourier transform $\hat{H}_\delta^p(\boldsymbol{k}) = \delta^{p+2}\hat{H}(\delta\boldsymbol{k})$,

and we obtain

$$C_\delta^p = C_0\delta^{2p+4}\int_{-\infty}^{\infty}\int_{-\infty}^{\infty}\frac{k^2}{\kappa}|\hat{H}(\delta\boldsymbol{k})|^2\,\mathrm{d}k\,\mathrm{d}l$$
$$= C_0\delta^{2p+1}\int_{-\infty}^{\infty}\int_{-\infty}^{\infty}\frac{(\delta k)^2}{\delta\kappa}|\hat{H}(\delta\boldsymbol{k})|^2\,\mathrm{d}\delta k\,\mathrm{d}\delta l = \delta^{2p+1}C. \tag{3.12}$$

Setting $p=-1/2$, we see that the conversion rate is invariant with respect to the simultaneous stretching and scaling $H(\boldsymbol{x}) \to H(\boldsymbol{x}/\delta)/\sqrt{\delta}$. For example, a given topography generates waves carrying the same amount of energy as the same topography shrunk by half (i.e. $\delta=1/2$) and amplified by $\sqrt{2}$.

3.2. *Solution using Green's function*

From (3.7) we have the horizontal convolution

$$W(\boldsymbol{x}, Z) = G(\boldsymbol{x}, Z) * \frac{\partial H}{\partial x}(\boldsymbol{x}), \tag{3.13}$$

where the causal Green's function is given by

$$G(\boldsymbol{x}, Z) = FT^{-1}\left\{\exp(-\mathrm{i}\kappa Z)\right\}. \tag{3.14}$$

This distribution can be computed as

$$G(\boldsymbol{x}, Z) = \frac{1}{(2\pi)^2}\int_{-\infty}^{\infty}\int_{-\infty}^{\infty}\mathrm{e}^{-\mathrm{i}\kappa Z}\mathrm{e}^{\mathrm{i}\boldsymbol{k}\cdot\boldsymbol{x}}\,\mathrm{d}k\,\mathrm{d}l = \frac{1}{2\pi}\int_0^{\infty}\kappa\mathrm{e}^{-\mathrm{i}\kappa Z}J_0(\kappa r)\,\mathrm{d}\kappa, \tag{3.15}$$

where $r=|\boldsymbol{x}|$ and J_0 is the zeroth-order Bessel function of the first kind. Hence

$$G(\boldsymbol{x}, Z) = \frac{\mathrm{i}}{2\pi}\frac{\partial}{\partial Z}\left(\int_0^{\infty}\mathrm{e}^{-\mathrm{i}\kappa Z}J_0(\kappa r)\,\mathrm{d}\kappa\right) \tag{3.16}$$
$$= \frac{\mathrm{i}}{2\pi r}\frac{\partial}{\partial Z}\left(\int_0^{\infty}\mathrm{e}^{-\mathrm{i}sZ/r}J_0(s)\,\mathrm{d}s\right) = \frac{\mathrm{i}}{2\pi r}\frac{\partial}{\partial Z}\tilde{J}(Z/r), \tag{3.17}$$

where $\tilde{J}(t)=\int_0^{\infty}J_0(s)\mathrm{e}^{-\mathrm{i}st}\,\mathrm{d}s$ is the one-dimensional Fourier transform of $J_0(s)\chi_{[0,\infty)}(s)$. The real and imaginary parts of $\tilde{J}$ can be found, for instance, in Watson (1966):

$$\tilde{J}(t) = \frac{\chi_{|t|<1}}{\sqrt{1-t^2}} - \mathrm{i}\left(\frac{-\chi_{t<-1}+\chi_{t>1}}{\sqrt{t^2-1}}\right),$$

where the indicator function $\chi_{t<-1}$ is one if $t<-1$ and so on. This yields

$$G(\boldsymbol{x}, Z) = G(r, Z) = \frac{1}{2\pi}\frac{\partial}{\partial Z}\left(\frac{\chi_{r<Z}}{\sqrt{Z^2-r^2}} + \mathrm{i}\frac{\chi_{r>Z}}{\sqrt{r^2-Z^2}}\right). \tag{3.18}$$

Convolution with this propagator $G(\boldsymbol{x}, Z)$ yields any wave field $A(\boldsymbol{x}, Z) = G(\boldsymbol{x}, Z) * A_0(\boldsymbol{x})$ in terms of its known values at the lower boundary $A_0(\boldsymbol{x}) = A(\boldsymbol{x}, 0)$, i.e.

$$A(\boldsymbol{x}, Z) = \frac{1}{2\pi}\frac{\partial}{\partial Z}\left(\iint\limits_{|\boldsymbol{x}'|<Z}\frac{A_0(\boldsymbol{x}-\boldsymbol{x}')}{\sqrt{Z^2-|\boldsymbol{x}'|^2}}\mathrm{d}x_1'\mathrm{d}x_2' + \mathrm{i}\iint\limits_{|\boldsymbol{x}'|>Z}\frac{A_0(\boldsymbol{x}-\boldsymbol{x}')}{\sqrt{|\boldsymbol{x}'|^2-Z^2}}\mathrm{d}x_1'\,\mathrm{d}x_2'\right) \tag{3.19}$$

where $\boldsymbol{x}'=(x_1', x_2')$. The first term is familiar from the Cauchy problem for the two-dimensional wave equation (with Z replacing time) but the second is not. If A_0 is real then (3.19) gives the explicit split of $A=A_r+\mathrm{i}A_i$ into its real and imaginary parts, where the real part is in phase with the tidal velocity and the imaginary part is out

of phase. Note that $A_r(\boldsymbol{x}, Z)$ depends on the boundary data $A_0(\boldsymbol{x}')$ for $|\boldsymbol{x}-\boldsymbol{x}'| \leqslant Z$, which is the interior of the circle centred at $\boldsymbol{x}$ and with radius Z. On the other hand, $A_i(\boldsymbol{x}, Z)$ depends on the boundary data $A_0(\boldsymbol{x}')$ for $|\boldsymbol{x}-\boldsymbol{x}'| \geqslant Z$, which is the exterior of the same circle. Clearly, the circle is the footprint of the characteristic backward cone with unit slope $\mathrm{d}Z/\mathrm{d}r$ and apex at $(\boldsymbol{x}, Z)$. Furthermore, in both cases the integrand is unbounded (although integrable) on the circle $|\boldsymbol{x}-\boldsymbol{x}'| = Z$, and this leads to the geometric focusing effects that will be studied in § 4.

For future reference we note that the Z-derivative in (3.19) can be incorporated in the integral if we introduce the integration variable $\boldsymbol{u} = (u_1, u_2) = \boldsymbol{x}'/Z$. After some manipulations and using the fact that A_0 is real (see (3.23) and (3.24) below), this leads to

$$A_r(\boldsymbol{x}, Z) = \frac{1}{2\pi} \iint\limits_{|\boldsymbol{u}|<1} \frac{A_0(\boldsymbol{x}-Z\boldsymbol{u}) - Z\boldsymbol{u}\cdot\nabla A_0(\boldsymbol{x}-Z\boldsymbol{u})}{\sqrt{1-|\boldsymbol{u}|^2}}\,\mathrm{d}u_1\,\mathrm{d}u_2, \tag{3.20}$$

$$A_i(\boldsymbol{x}, Z) = \frac{1}{2\pi} \iint\limits_{|\boldsymbol{u}|>1} \frac{A_0(\boldsymbol{x}-Z\boldsymbol{u}) - Z\boldsymbol{u}\cdot\nabla A_0(\boldsymbol{x}-Z\boldsymbol{u})}{\sqrt{|\boldsymbol{u}|^2-1}}\,\mathrm{d}u_1\,\mathrm{d}u_2. \tag{3.21}$$

We now turn to computing the overturning amplitude at the lower boundary. The non-dimensional overturning amplitude A is again defined by

$$\frac{\partial\Theta}{\partial Z} = \frac{N^2}{\mu}\left\{1 - \mathrm{Re}\left[\mathrm{e}^{-\mathrm{i}\omega_0 t} A(\boldsymbol{x}, Z)\right]\right\}. \tag{3.22}$$

In Fourier space the wave amplitude at $Z=0$ is found to be

$$\hat{A}_0(\boldsymbol{k}) = \frac{U_0 h_0 \mu}{\omega_0}\,\kappa\,\mathrm{i}k\hat{H}(\boldsymbol{k}) \tag{3.23}$$

and therefore we obtain the alternative real-space expressions

$$\frac{\omega_0}{U_0 h_0 \mu} A_0(\boldsymbol{x}) = \sqrt{-\Delta}\left[\frac{\partial H}{\partial x}\right] = \frac{\partial}{\partial x}\left\{\frac{-1}{2\pi r} * \Delta H(\boldsymbol{x})\right\} = \frac{x}{2\pi r^3} * \Delta H(\boldsymbol{x}) \tag{3.24}$$

for A_0 in terms of the topography H. (See Chapter V of Stein 1970 for some properties of the fractional Laplacian operator $\sqrt{-\Delta}$; also, the convolution expressions make use of $FT^{-1}\{1/\kappa\} = 1/(2\pi r)$ and the final convolution must be evaluated in the principal value sense.) Note that A_0 is real and therefore the overturning amplitude at the bottom is in phase with the tide, as it was in the two-dimensional case.

We illustrate (3.24) by computing $A_0(\boldsymbol{x})$ for the Gaussian bump topography $H(\boldsymbol{x}) = \exp(-|\boldsymbol{x}|^2/2\sigma^2)/(2\pi\sigma^2)$ with $\sigma = 0.5$ as shown in figure 3. The amplitude $A_0(\boldsymbol{x})$ is maximal at a point on the x-axis with $x<0$, i.e. before the Gaussian bump in the tidal direction. This can be most easily understood from the final convolution in (3.24) together with $\Delta H < 0$ in the core of the Gaussian. Hence $A_0(\boldsymbol{x})\cos(\omega_0 t)$ for $\omega_0 t = 0$ has a maximum at $x<0$, whilst for $\omega_0 t = \pi$ its maximum is at $x>0$. In any case, $A_0(\boldsymbol{x})\cos(\omega_0 t)$ is maximum on the side of the topography from which the tidal current is coming. Therefore overturning instabilities at the bottom will again arise on the upwind side of the topography relative to the tidal current.

In figure 4 we illustrate the interior amplitude $A(\boldsymbol{x}, Z)$† for the same Gaussian bump topography. The real part of A is maximal at the lower boundary $Z=0$. However,

† Here and in the following the wave solution was evaluated using a Fourier series on a large three-dimensional grid with typical resolution $\mathrm{d}x = \mathrm{d}y = \mathrm{d}Z = 0.05\sigma$.

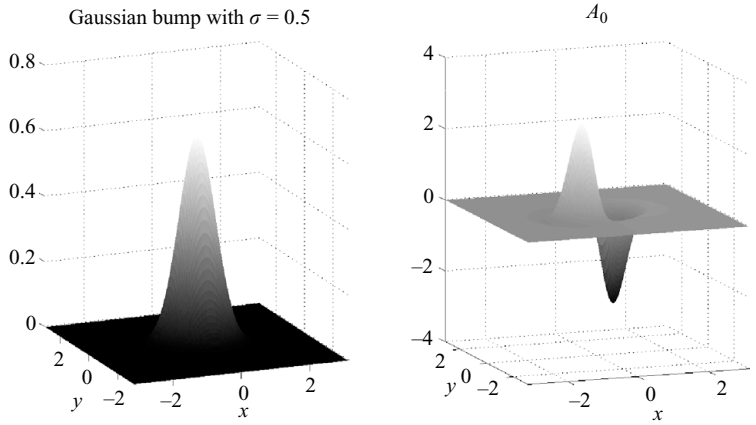

FIGURE 3. Qualitative amplitude of the wave field generated at $Z = 0$ by a Gaussian bump with $U_0 h_0 \mu/\omega_0 = 1$ for ease of plotting. The x-axis is aligned with the tidal flow and the overturning amplitude is in phase with tidal flow and largest on the upwind side of the bump.

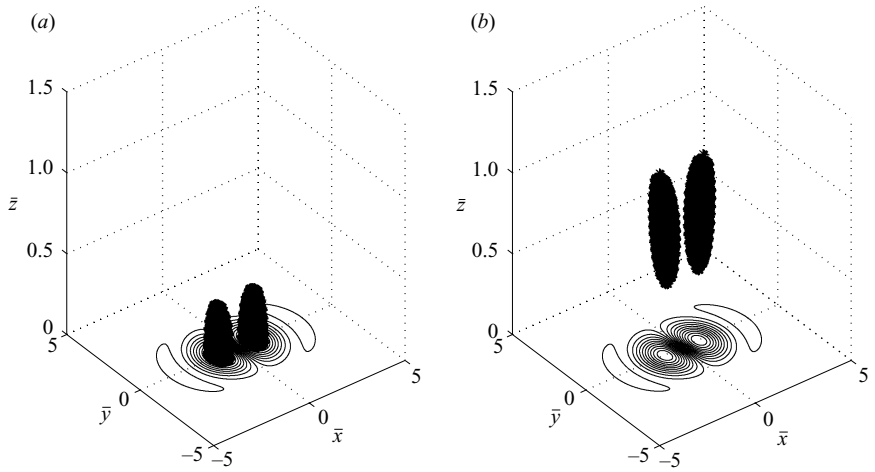

FIGURE 4. Real (a) and imaginary (b) part of $A(\boldsymbol{x}, Z)$ for Gaussian bump topography with width σ. The boundary amplitude A_0 is contoured in terms of the scaled coordinates $(\bar{x}, \bar{y}) = (x/\sigma, y/\sigma)$. The markers indicate grid locations where $|A_r|$ and $|A_i|$ are within 20 % of their maximal values, respectively. The real part achieves its maximal value at the boundary whereas the imaginary part achieves its maximum in the interior, roughly at $Z = 0.75\sigma$. The maximal value of $|A_i|$ is about 90 % of the maximal value of $|A_r|$ for Gaussian topography.

the imaginary part of A is maximal in the interior, broadly at a distance $Z > 0$ that is proportional to the topography width σ (see caption for details). Both amplitude maxima are closely comparable in magnitude and therefore wave breaking, should it occur, is likely to arise both at the boundary and in the ocean interior.

In the remainder of the paper we will consider only the dependence of the interior wave amplitude $A(\boldsymbol{x}, Z)$ on the shape of a given boundary amplitude field $A_0(\boldsymbol{x})$. In other words, we separate conceptually and computationally the wave generation part of the problem, which is described by the relation between $A_0(\boldsymbol{x})$ and $H(\boldsymbol{x})$ in (3.24), from the wave propagation part, which is described by the relation between $A(\boldsymbol{x}, Z)$ and $A_0(\boldsymbol{x})$ in (3.19). The latter part can lead to wave focusing, which we study now.

4. A three-dimensional effect: focusing

The interior wave amplitude A is given by the action of the propagator on A_0, i.e. $A(\boldsymbol{x}, Z) = G(\boldsymbol{x}, Z) * A_0(\boldsymbol{x})$. Our task in this section is to understand how simple boundary configurations of A_0 are propagated into the interior, and especially under what circumstances interior amplitudes can be significantly enhanced locally when compared to the boundary amplitudes. This has an impact on the three-dimensional distribution of likely wave instability and wave breaking. To begin with, it is a simple consequence of $|\hat{G}| = 1$ that the propagation map is unitary in the sense of a constant quadratic norm, i.e.

$$\int |A(\boldsymbol{x}, Z)|^2 \,\mathrm{d}x\mathrm{d}y = \int \left(A_r^2 + A_i^2\right) \mathrm{d}x\mathrm{d}y = \int |A_0(\boldsymbol{x})|^2 \,\mathrm{d}x\mathrm{d}y. \tag{4.1}$$

In other words, the root-mean-square value of A is independent of Z. As noted in the Introduction, the constancy of this quadratic norm for A masks the possible non-uniformity of A in space, i.e. the possibility of large $|A|$ in some localized region. Wave breaking is caused by local wave amplitudes exceeding an instability threshold, and therefore wave breaking is likely to be non-uniform in space in a manner that is analogous to A. This non-uniformity is clearly not captured by the root-mean-square value of A and therefore we must look more closely into the anatomy of the propagator G.

For instance, we would like to have a qualitative understanding of the interior amplitude distribution in response to Gaussian topography, which was displayed in figure 4. In particular, we want to understand how this interior distribution is related to the dipolar and curved distribution of boundary amplitude, which is contoured in the same plot. To this end we will look at a few very simple examples of A_0 distributions and develop a geometric theory to understand the interior amplitudes that arise in these examples. We can then use these building blocks to understand more complex distributions by superposition.

There is one technical point that needs to be noted at this stage. It is clear from the x-derivative in the generation formula (3.24) that A_0 satisfies the integral constraint $\int A_0(x, y)\mathrm{d}x = 0$ for all y. It is convenient to dispense with this constraint when considering simple shapes of A_0 such as a monopolar bump. In other words, it is tacitly understood from now on that a realistic A_0 can be assembled by a suitable superposition of simple shapes that together satisfy the integral constraint.

4.1. *Geometric theory for Gaussian boundary amplitude*

A direct look at A in terms of simple shapes in A_0 is complicated by the singularities of G that are apparent in (3.18). These singularities disappear once G is convolved with a smooth A_0 and therefore it is natural to consider a monopolar Gaussian bump in A_0 such that

$$A_0(\boldsymbol{x}) = \frac{\alpha}{2\pi\sigma^2} \mathrm{e}^{-|\boldsymbol{x}|^2/(2\sigma^2)} \quad \text{with} \quad \alpha = \frac{U_0 h_0 \mu}{\omega_0}. \tag{4.2}$$

As the width $\sigma \to 0$, $G * A_0$ goes to G in the sense of distributions (up to an α factor), hence understanding the action of G on a Gaussian bump will help us understand its action on arbitrary topography. By horizontal isotropy, A is radially symmetric in $\boldsymbol{x}$, i.e. $A(\boldsymbol{x}, Z) = A(r, Z)$ where $r = |\boldsymbol{x}|$. Furthermore, from (3.14) we have the homogeneity relation $\sigma^2 G(r, Z) = G(r/\sigma, Z/\sigma)$ for all $\sigma > 0$ and it then follows from (4.2) that

$$A(r, Z) = \frac{\alpha}{2\pi\sigma^2} f\,(r/\sigma, Z/\sigma) \quad \text{where} \quad f(\bar{r}, \bar{Z}) = G(\bar{r}, \bar{Z}) * \mathrm{e}^{-\bar{r}^2/2} \tag{4.3}$$

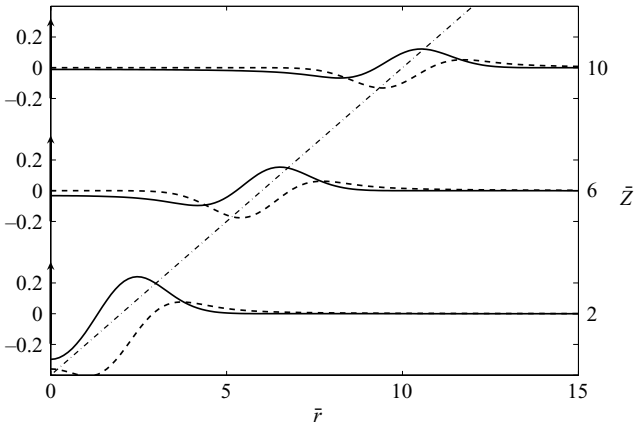

FIGURE 5. Real part (plain line) and imaginary part (dashed line) of $f(\bar{r}, \bar{Z}) = G(\bar{r}, \bar{Z}) * \mathrm{e}^{-\bar{r}^2/2}$ versus $\bar{r}$ for different values of $\bar{Z}$. The line $\bar{r} = \bar{Z}$ is also shown (dot-dashed). We see that at a given $\bar{Z}$, the function has a front around $\bar{r} = \bar{Z}$. In fact, the real part of f is exactly zero after the front and the imaginary part is zero before the front, as expected from the integration domains in (3.20) and (3.21). We also see that the magnitude of f decreases with height.

and the final convolution is taken over $(\bar{x}, \bar{y})$. Hence decreasing σ corresponds to compressing the support and amplifying the magnitude of both A and A_0. In particular, $|A(\boldsymbol{x}, Z)|_{\max} \propto 1/\sigma^2$.

Now, in principle a monopolar distribution of A_0 centred at the origin produces a non-zero $A \propto f(r/\sigma, Z/\sigma)$ at all r and $Z > 0$. In other words, the domain of influence of the boundary point $(\boldsymbol{x}, Z) = (0, 0, 0)$ is the entire open half-space $Z > 0$. However, the interior amplitude distribution due to a monopolar A_0 is strongly concentrated in the neighbourhood of the characteristic forward cone, which has apex at $(\boldsymbol{x}, Z) = (0, 0, 0)$ and slope $\mathrm{d}Z/\mathrm{d}r$ equal to unity.

This is apparent from the real and imaginary parts of f that are plotted in figure 5 versus $\bar{r}$ at various $\bar{Z}$. We see that the function f has a front at the forward cone $\bar{r} = \bar{Z}$. More precisely, its real part has a positive extremum just after $\bar{r} = \bar{Z}$, its imaginary part has a negative extremum just before $\bar{r} = \bar{Z}$, and these extrema decrease in magnitude with $\bar{Z}$. With a little more effort (see (4.5) below), it can be shown that the extrema decay as $1/\sqrt{\bar{Z}}$ if $\bar{Z} \gg 1$, which is consistent with the usual far-field behaviour of solutions to the two-dimensional wave equation, Z replacing time. The important observation is that the second, imaginary part of the propagator in (3.19) shows the same behaviour.

This suggests a geometric theory for the far-field behaviour of the propagator G such that smooth boundary data A_0 at a point $\boldsymbol{x}'$, say, induces an interior amplitude A only on the forward cone $(\boldsymbol{x}, Z)$ such that $|\boldsymbol{x} - \boldsymbol{x}'| = Z$ and that along this cone the induced amplitude decays as $1/\sqrt{Z}$. This geometric theory is an approximation to the full propagator and it is accurate at distances from the boundary that are large compared to the gradient scale of the topography, which is σ in the case of the Gaussian bump.

We will use this geometric theory to understand the interior amplitude response to more complicated boundary data, but before this we briefly show how to compute the asymptotic decay rate of the amplitude on the forward cone as a function of altitude, i.e. we estimate how $f(\bar{Z}, \bar{Z})$ varies with $\bar{Z}$ for $\bar{Z} \gg 1$. From (4.3) and (3.20)–(3.21) we

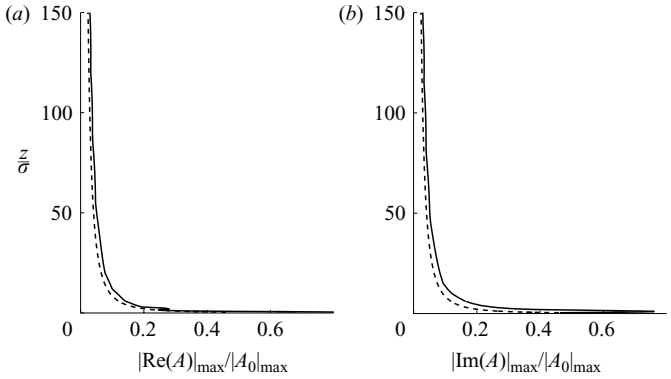

FIGURE 6. (*a*) $\max_{\{\bar{r}\geqslant 0\}}|\mathrm{Re}(f(\bar{r},\bar{Z}))| = \max_{\{r\geqslant 0\}}|\mathrm{Re}(A(r,Z))|/|A_0|_{\max}$ (plain line) and (*b*) $\max_{\{\bar{r}\geqslant 0\}}|\mathrm{Im}(f(\bar{r},\bar{Z}))| = \max_{\{r\geqslant 0\}}|\mathrm{Im}(A(r,Z))|/|A_0|_{\max}$ (plain line) versus $\bar{Z} = Z/\sigma$. The dashed line is the asymptotic behaviour obtained with Laplace's method. We see that, the real and imaginary parts are in good agreement with the asymptotics. In particular we see that, for fixed σ, the amplitude of the wave field decays like $1/\sqrt{Z}$ as $Z \to \infty$.

obtain

$$\mathrm{Re}(f(\bar{Z},\bar{Z})) = \frac{1}{2\pi}\int_{u=0}^{1}\int_{\theta=-\pi}^{\pi}\frac{\mathrm{e}^{-\bar{Z}^2(1+u^2-2u\cos\theta)/(2)}}{\sqrt{1-u^2}}(1+\bar{Z}^2u(\cos\theta-u))\,\mathrm{d}\theta\,u\,\mathrm{d}u$$

and

$$\mathrm{Im}(f(\bar{Z},\bar{Z})) = \frac{1}{2\pi}\int_{1}^{\infty}\int_{-\pi}^{\pi}\frac{\mathrm{e}^{-\bar{Z}^2(1+u^2-2u\cos\theta)/2}}{\sqrt{u^2-1}}(1+\bar{Z}^2u(\cos\theta-u))\,\mathrm{d}\theta\,u\,\mathrm{d}u. \tag{4.4}$$

Using Laplace's method we derive the following asymptotic behaviour for $\bar{Z} \gg 1$ (e.g. chapter 6 of Bender & Orszag 2005; details are found in Appendix C):

$$f(\bar{Z},\bar{Z}) \approx (1-\mathrm{i})\,\frac{2^{-5/4}\pi^{-1/2}\,\Gamma(3/4)}{\bar{Z}^{1/2}}. \tag{4.5}$$

Here Γ denotes the gamma function $\Gamma(s) = \int_0^\infty u^{s-1}\mathrm{e}^{-u}\,\mathrm{d}u$. Note that the real and imaginary parts of f have same maximal magnitudes, but the real part has a positive extremum, and the imaginary part has a negative extremum, consistent with what we observed on figure 5. Figure 6 shows the maximum magnitudes of the real part (*a*) and imaginary part (*b*) of f at different heights $\bar{Z} = Z/\sigma$. The dashed line is the asymptotic estimate derived with Laplace's method. We see that the real and imaginary parts of f are in good agreement with the asymptotics. Note that the asymptotic estimate is a little below the actual extrema. This is not surprising since we derived asymptotics for $|f(\bar{Z},\bar{Z})|$, using the fact that at given $\bar{Z}$, $\max_{\{\bar{r}\geqslant 0\}}|f(\bar{r},\bar{Z})| \approx |f(\bar{Z},\bar{Z})|$. In reality, as seen in figure 5, the extrema of f do not occur exactly at the front $\bar{r} = \bar{Z}$, but just after the front for the real part and right before the front for the imaginary part.

For ease of reference, the corresponding asymptotic expression for the overturning amplitude is

$$A(Z,Z) \approx (1-\mathrm{i})\,\frac{\alpha}{2\pi\sigma^2}\,\frac{2^{-5/4}\Gamma(3/4)}{(\pi Z/\sigma)^{1/2}}. \tag{4.6}$$

The prefactor $\alpha/2\pi\sigma^2$ equals the maximum of A_0 at the boundary. Finally, by combining (3.22) and (4.3), (4.5) we find that the real-valued time-dependent amplitude

on the forward cone is asymptotically equal to the real part of (4.6) times $\sqrt{2}\cos(\omega_0 t + \pi/4)$, which lags the tidal oscillation by an eighth of a period.

As in § 2.3, it is noteworthy how the present wave structure differs from that of lee waves. For three-dimensional hydrostatic non-rotating lee waves one readily obtains $m = (\kappa/k)N/U$. The vertical displacement of the isopycnals is $\eta(\boldsymbol{x}, 0) = h(\boldsymbol{x})$ at the bottom, and there is anisotropic vertical propagation $\hat{\eta}(\boldsymbol{k}, z) = \exp(\mathrm{i}mz)\hat{\eta}(\boldsymbol{k}, 0)$. Three-dimensional lee waves are again localized over isolated topography, although there is now also a bow-wave pattern that curves and extends leewards. This is in sharp contrast to the isotropic front-like spreading shown in figure 5.

4.2. *Point focusing from circular boundary data*

The geometric theory for the interior amplitude makes obvious that for distributed boundary data there can be geometric focusing effects at the envelopes formed by the various forward cones. For instance, consider the simplest, albeit non-generic, focusing structure, which is due to boundary data supported on a circular ring with radius R centred at the origin, say. In the geometric theory the boundary data located at any $\boldsymbol{x}'$ contributes to $A(\boldsymbol{x}, Z)$ only on the corresponding forward cone, which at fixed $Z > 0$ is a circle with radius Z and centre $\boldsymbol{x}'$. Hence the various propagated contributions from circular boundary data supported on $|\boldsymbol{x}'| = R$ intersect at the point $(0, 0, R)$ above the centre of the circle and we expect $|A|$ to be amplified there. This geometric focusing effect can lead to interior amplitudes that exceed the boundary amplitudes.

We illustrate this with a simple Gaussian ring in boundary amplitude defined by

$$A_0(\boldsymbol{x}) = \frac{\alpha}{2\pi\sigma^2}\mathrm{e}^{-(|\boldsymbol{x}|-R)^2/2\sigma^2} = \frac{\alpha}{2\pi\sigma^2}\mathrm{e}^{-d^2/2\sigma^2}, \tag{4.7}$$

where d is the distance from $\boldsymbol{x}$ to the circle $x^2 + y^2 = R^2$. Clearly, these boundary data can be thought of as the continuous limit of arrangements in which many Gaussian bumps with width σ are distributed around this circle.

Using the same argument as in (4.3), it follows that

$$\left.\begin{aligned} &A(r, Z) = \frac{\alpha}{2\pi\sigma^2}\, g\,(r/\sigma, Z/\sigma) = |A_0(\boldsymbol{x})|_{\max}\; g\,(r/\sigma, Z/\sigma) \\ &g(\bar{r}, \bar{Z}) = G(\bar{r}, \bar{Z}) * \mathrm{e}^{-(\bar{r}-\bar{R})^2/2}, \text{ and } \quad \bar{R} = R/\sigma. \end{aligned}\right\} \tag{4.8}$$

Figure 7 shows the locations of maximal magnitudes of $\mathrm{Re}(g)$ (stars) and $\mathrm{Im}(g)$ (circles) for $\bar{R} = 10$. The boundary data $\mathrm{e}^{-(\bar{r}-\bar{R})^2/2}$ are displayed at $\bar{Z} = 0$ together with a sketch of the forward cones in a cross-section.

We observe that the points where g is maximal are indeed located near the point of intersection of the forward cones at $(\bar{x}, \bar{y}, \bar{Z}) = (0, 0, \bar{R})$. Specifically, the real part of A has a positive extremum just below the point of intersection and its imaginary part has a negative extremum right above the point of intersection. This is consistent with the locations of the fronts in figure 5. Quantitatively, we find that $|\mathrm{Re}(g)|_{\max} = |A_r|_{\max}/|A_0|_{\max} \approx 3$ and $|\mathrm{Im}(g)|_{\max} = |A_i|_{\max}/|A_0|_{\max} \approx 3$. These ratios are greater than unity and hence in this example it is true that the wave field could be stable at the boundary and yet be unstable at the interior focusing point.

We can make a simple estimate for the amplitude at the focusing point in the regime $R \gg \sigma$, where the radius of the Gaussian ring is much larger than its width. In this regime the far-field asymptotics of § 4.1 are applicable in the focusing region. We now think of the circular amplitude (4.7) as a superposition of Gaussian bumps located on a circle of radius R. The volume of the Gaussian ring is

$$V_c = \frac{1}{2\pi\sigma^2}\int_{-\infty}^{\infty}\int_{-\infty}^{\infty}\mathrm{e}^{-(|\boldsymbol{x}|-R)^2/(2\sigma^2)}\mathrm{d}x\,\mathrm{d}y \approx \frac{R}{\sigma}\sqrt{2\pi} \text{ for } \frac{R}{\sigma} \gg 1. \tag{4.9}$$

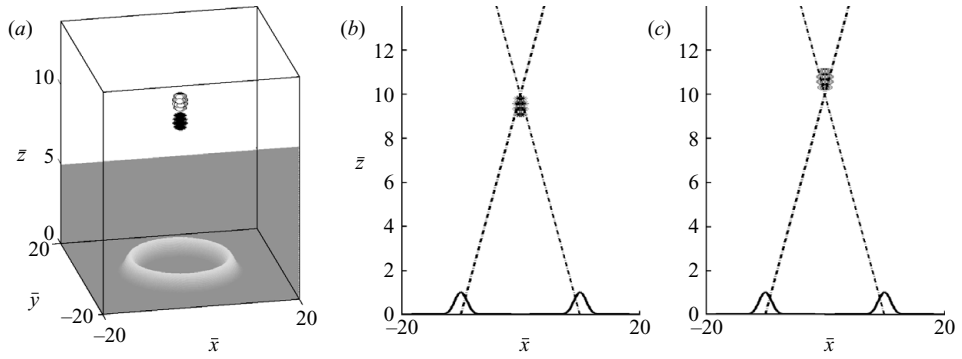

FIGURE 7. (*a*) Points where $|\mathrm{Re}(g(\bar{r}, \bar{Z}))|/|\mathrm{Re}(g)|_{\max} > 80\,\%$ (stars) and where $|\mathrm{Im}(g(\bar{r}, \bar{Z}))|/|\mathrm{Im}(g)|_{\max} > 80\,\%$ (circles), as functions of $\bar{x}$, $\bar{y}$ and $\bar{Z}$ ($\bar{r} = |(\bar{x}, \bar{y})|$). In this example, $\bar{R} = 10$. The boundary data $\mathrm{e}^{-(\bar{r}-\bar{R})^2/2}$ are displayed at $\bar{Z} = 0$. (*b*) and (*c*), cross-sections in the $\bar{y} = 0$ plane of (*a*), show the forward cones (dot-dashed) emanating from $|\boldsymbol{x}| = R$. The region of maximal amplitudes is located near $(0, 0, \bar{R})$, as expected.

Now, the amplitude at the focusing point $(0, 0, R)$ can be approximated by the superposition of individual contributions from Gaussian bumps that are located at horizontal distance R and have combined volume V_c. The volume of a single Gaussian bump is unity and therefore we simply need to multiply V_c by the asymptotic expression for a single Gaussian bump in (4.6) with $Z = R$. It can be checked that this argument leads to the same estimate as applying Laplace's method to the convolution integral. The result is

$$A(0, R) \approx (1 - \mathrm{i})\,\frac{\alpha}{2\pi\sigma^2} 2^{-3/4} \Gamma(3/4) \sqrt{\frac{R}{\sigma}}. \tag{4.10}$$

Again, $\alpha/2\pi\sigma^2 = |A_0(\boldsymbol{x})|_{\max}$ and the real-valued time-dependent amplitude at the focusing point is approximated by the real part of (4.10) times $\sqrt{2}\cos(\omega_0 t + \pi/4)$. The amplification at the focusing point is measured by $g(0, \bar{R}) = A(0, \bar{R}\sigma)/|A_0(\boldsymbol{x})|_{\max} \approx (1-\mathrm{i})2^{-3/4}\Gamma(3/4)\bar{R}^{1/2}$, which indicates that the amplification is proportional to $\sqrt{R/\sigma}$. This is illustrated in figure 8, which shows the approximated amplification factor as a function of $\bar{R}$ and compares it with numerical results for the global maximum of g.

There is reasonable agreement between the curves, although the approximation falls noticeably short of the numerical values. For instance, in the example with $\bar{R} = 10$ the numerical amplification factor was $3(1 - \mathrm{i})$, whereas the approximation yields only $2.3(1 - \mathrm{i})$. Part of the disagreement is because we approximated $A(0, R)$, whereas the actual maximum amplitudes do not occur exactly at $Z = R$, but slightly below for the real part and slightly above for the imaginary part, as seen in figure 7.

Finally, we have also computed the wave field for the case of a circular ridge. In this case the actual *topography* $H(\boldsymbol{x})$ has the circular shape (4.7) and the corresponding amplitude $A_0(\boldsymbol{x})$ is determined from the general relation (3.23). We find that substantial amplification of boundary amplitudes by focusing occurs just as before, with amplification factors that are within 20 % of those found in this section.

Moving on, we note that the present example is non-generic in the sense that the perfectly circular amplitude configuration on the boundary led to focusing in a single point in the interior. Generically, we expect that the focusing point is smeared out into a focusing line once the boundary amplitude is supported on less symmetric

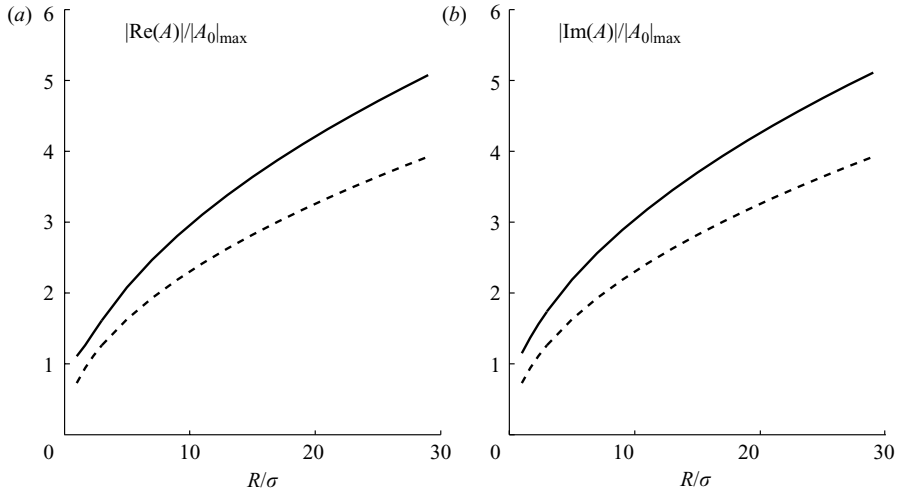

FIGURE 8. (*a*) The amplification factor $\max_{\{\bar{r},\bar{Z}\}} |\mathrm{Re}(g(\bar{r},\bar{Z}))| = \max_{\{r,Z\}} |\mathrm{Re}(A(r,Z))|/|A_0|_{\max}$ and (*b*) $\max_{\{\bar{r},\bar{Z}\}} |\mathrm{Im}(g(\bar{r},\bar{Z}))| = \max_{\{r,Z\}} |\mathrm{Im}(A(r,Z))|/|A_0|_{\max}$, versus $\bar{R}$. The asymptotic estimate is displayed as a dashed line and values above unity indicate interior amplitudes that are above boundary amplitudes.

structures. This generic set-up reduces but does not eradicate the amplification due to focusing, as we shall describe in the next section.

4.3. *Line focusing from elliptical boundary data*

We continue to consider boundary amplitude data that are supported on smooth strips with width σ. In the previous section the strip was a perfectly circular ring with radius R and the focusing region was the centre point of this circle translated vertically to altitude $Z = R$. This example was non-generic because the radius of curvature was constant along the strip, i.e. $R(s)$ is constant if s measures arclength along the centreline of the strip, say. However, we can generalize this example to strips with variable radius of curvature $R(s)$ by assuming that each segment of the strip leads to focusing in a location that lies at a horizontal distance $R(s)$ normal to the segment under consideration and is also translated by a distance $R(s)$ in the vertical. In other words, we expect a focusing effect near the Z-translated evolute of the boundary data. By evolute we mean the set of all the centres of curvature of the supporting strip (this is equivalent to the envelope of the normals), and by Z-translated we mean translated vertically to $Z = R(s)$, which is the local radius of curvature. This construction leads to a line as the generic focusing set and the Z-translation makes clear that this line has a non-trivial shape in three dimensions.

The simplest strip example with non-constant curvature is the case where the centreline is an ellipse, whose evolute is known as the Lamé curve. This curve is shown in figure 9(*a*) (dashed black curve) for an ellipse with semi-major axis 14 and semi-minor axis 10. When we Z-translate the Lamé curve we obtain the dashed black curves shown in figures 9(*b*) and 9(*c*). Due to geometric focusing, we hence expect the amplitude to be largest near this Z-translated evolute.

We check this with the elliptic boundary amplitude

$$A_0(\boldsymbol{x}) = \frac{\alpha}{2\pi\sigma^2} \mathrm{e}^{-d^2/2\sigma^2}, \tag{4.11}$$

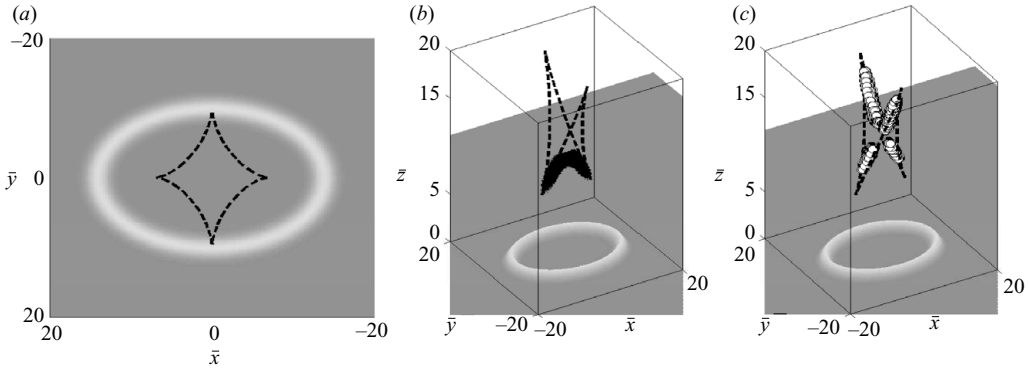

FIGURE 9. Points where $|\mathrm{Re}(h(\bar{x}, \bar{y}, \bar{Z}))|/|\mathrm{Re}(h)|_{\max} > 80\,\%$ (stars in panel b) and where $|\mathrm{Im}(h(\bar{x}, \bar{y}, \bar{Z}))|/|\mathrm{Im}(h)|_{\max} > 80\,\%$ (circles in panel c), as functions of $\bar{x}$, $\bar{y}$ and $\bar{Z}$. The boundary data $\mathrm{e}^{-\bar{d}^2/2}$ are displayed at $\bar{Z} = 0$. In this example, $\bar{a} = 14$ and $\bar{b} = 10$, and the dashed black curve is the evolute of the ellipse translated vertically to the radius of curvature. We see that points of maximal h are indeed located near this curve.

where d is the distance from $\boldsymbol{x}$ to the ellipse $x^2/a^2 + y^2/b^2 = 1$. Again, we have that

$$\left.\begin{aligned} A(\boldsymbol{x}, Z) &= \frac{\alpha}{2\pi\sigma^2} h\,(\boldsymbol{x}/\sigma, Z/\sigma) = |A_0(\boldsymbol{x})|_{\max}\; h\,(\boldsymbol{x}/\sigma, Z/\sigma) \\ h(\bar{\boldsymbol{x}}, \bar{Z}) &= G(\bar{\boldsymbol{x}}, \bar{Z}) * \mathrm{e}^{-\bar{d}^2/2} \end{aligned}\right\} \quad \text{where} \tag{4.12}$$

and $\bar{d}$ denotes the distance from $\bar{\boldsymbol{x}}$ to the ellipse with scaled semi-axes $\bar{a} = a/\sigma$ and $\bar{b} = b/\sigma$. Figure 9 shows numerical results for the locations of maximal magnitudes of $\mathrm{Re}(h)$ (stars in figure 9b) and $\mathrm{Im}(h)$ (circles in figure 9c) for $\bar{a} = 14$ and $\bar{b} = 10$. The boundary data are displayed at $\bar{Z} = 0$, and the evolute of the ellipse with semi-major axis $\bar{a}$ and semi-minor axis $\bar{b}$ is shown as a dashed black curve. The evolute is translated vertically to the radius of curvature in the three-dimensional panels.

We observe that, indeed, h is maximal near this translated evolute. Quantitatively, we find the amplification factors $|\mathrm{Re}(h)|_{\max} = |A_r|_{\max}/|A_0|_{\max} \approx 1.7$ and $|\mathrm{Im}(h)|_{\max} = |A_i|_{\max}/|A_0|_{\max} \approx 1.6$. This verifies that focusing can lead to increased interior amplitudes near the line-like locations predicted by the geometric theory.

5. Concluding remarks

We have shown that the formation of unstable wave regions can be remarkably non-uniform even for very simple idealized sea-floor topography. This is due both to the peculiar boundary conditions of the present wave problem as well as the focusing effect in three-dimensional flow. Overall, this work is part of an on-going project aimed at providing a theory for the vertical distribution of wave breaking and diffusivity over irregular sea-floor topography.

Within the confines of linear theory for sub-critical topography the present study could be made more realistic by allowing for finite tidal excursions (see Appendix B below), for variable stratification, and for a finite ocean depth. Arguably, it is the extension to finite ocean depth that has the most dramatic impact both on the general tides problem and also on the interior wave focusing studied here. Indeed, with a typical characteristic slope $\mu^{-1} \approx 0.2$, focusing may lead to pockets of enhanced mixing in the bottom two kilometres of the ocean only for curved topographic features of horizontal extent less than about 10 kilometres. This is below the current resolution

of the global bathymetry (Smith & Sandwell 1997). For larger topography features the characteristics are back-reflected at the upper boundary $z = H$, say, where the vertical fluid velocity of the internal tides vanishes to a very good approximation. The characteristics are also reflected at the ocean floor $z = 0$ and the resulting structure of the solution changes considerably because of the cumulative nature of successive up–down reflections. Specifically, it is easy to derive that for finite H the Fourier transforms of the vertical velocity and of the wave amplitude at the sea floor are related by $\hat{A}_0 = -(\mathrm{i}\mu\kappa/\omega_0)\cot(\mu\kappa H)\,\hat{w}_0$, and that their respective three-dimensional structures are given by

$$\hat{A}(\boldsymbol{k}, z) = \frac{\cos(\mu\kappa(H-z))}{\cos(\mu\kappa H)}\,\hat{A}_0(\boldsymbol{k}), \quad \hat{w}(\boldsymbol{k}, z) = \frac{\sin(\mu\kappa(H-z))}{\sin(\mu\kappa H)}\,\hat{w}_0(\boldsymbol{k}). \tag{5.1}$$

Here z is the unscaled altitude above the sea floor. There is now a possibility of resonance with ocean normal modes whenever $\mu\kappa H$ is a multiple of π. Also, even for compact topography any numerical simulation of (5.1) on a periodic domain suffers from sensitive dependence of the solution to small changes in the domain size; this is an echo of the well-known ill-posedness of the boundary-value problem for time-periodic internal waves in general bounded domains (e.g. Sobolev 1960; Maas & Lam 1995).

The solution for finite H can be regularized by introducing dissipation along the characteristics, which in (5.1) can be achieved by replacing κ by $\kappa(1 - \mathrm{i}\epsilon)$ with a small positive ϵ that may depend on κ.† For instance, with weak dissipation in place we have considered a circular boundary amplitude with radius R as in §4.2, but with finite ocean depth such that $\mu H < R$. Our preliminary results indicate that focusing regions are still formed by the characteristic cones once reflections at the ocean boundaries are taken into account. Specifically, the vertical position of focusing regions is affected by the reflections, but their horizontal position remains unchanged at the centres of curvature related to the topography shape. This makes focusing relevant for considerably larger topographic shapes.

The need for dissipation along characteristics brings up the question of how to model the dissipation due to wave saturation and breaking. We currently plan to use the Green's function of this paper to build a model for the effect of wave saturation on the wave field. Briefly, at any altitude z we can constrain the wave amplitude field to lie below unity, which models the turbulent saturation of the unstable wave field. The Green's function can then be used to propagate the saturated wave field further in altitude, leading to further breaking regions and saturation. In this way an estimate for the vertical distribution of wave breaking and turbulent mixing can be formulated, which could be used to constrain parametrization models in large-scale numerical models for the ocean.

This investigation also suggests the natural use of random topography with an energy spectrum constrained by the data. For instance, the internal tides generated by two-dimensional Gaussian random topography are a three-dimensional Gaussian random field themselves, with easily studied geometric properties for the formation of regions of high wave amplitude, for example. This could be useful in order to investigate the likely importance of unobservable sub-grid-scale topography on the wave breaking distribution in the deep ocean.

† Alternatively, one can study the well-posed initial-value problem in which ω_0 is replaced by $\omega_0 + \mathrm{i}\alpha$, where $\alpha > 0$ is a growth rate small compared to ω_0. This yields $\epsilon = \alpha\omega_0 N^2/((\omega_0^2 - f^2)(N^2 - \omega_0^2))$ if $N \gg f$, and so in this case ϵ does not depend on κ.

It is a pleasure to acknowledge fruitful discussions of this work with Esteban Tabak and Bruno Voisin. The comments of several referees helped improve the paper. Financial support for this work under the National Science Foundation grants OCE-0324934 and DMS-0604519 is gratefully acknowledged.

Appendix A. Computation of the Green's function in the two-dimensional case

From (2.10), the Green's function is given by $G(x, Z) = FT^{-1}\{e^{-i|k|Z}\}$. In order to compute $G(x, Z)$, it is convenient to get rid of the absolute value. To this end, we use the Heaviside function denoted H_v, and write

$$\hat{G}(k, Z) = e^{-i|k|Z} = H_v(k)e^{-ikZ} + H_v(-k)e^{ikZ}. \tag{A 1}$$

Hence

$$\begin{aligned} G(x, Z) &= FT^{-1}\{H_v(k)e^{-ikZ}\}(x) + FT^{-1}\{H_v(-k)e^{ikZ}\}(x) \\ &= FT^{-1}\{H_v\}(x - Z) + FT^{-1}\{H_v(-.)\}(x + Z) \\ &= FT^{-1}\{H_v\}(x - Z) + FT^{-1}\{H_v\}(-x - Z). \end{aligned}$$

In the sense of distributions $FT^{-1}\{H_v\}(x) = i/(2\pi x) + \delta(x)/2$ and

$$G(x, Z) = \frac{1}{2}(\delta(x + Z) + \delta(x - Z)) + \frac{i}{2\pi}\left(\frac{1}{x - Z} - \frac{1}{x + Z}\right). \tag{A 2}$$

Appendix B. Amplitude for finite tidal excursion

B.1. *Two-dimensional flow over one-dimensional topography*

Our purpose here is to compute the amplitude of the wave field for finite tidal excursion, i.e. without the assumption (2.1). We first consider the two-dimensional problem and we use the same notation as in § 2. In this regime, advection by the tides can not be neglected and $\partial/\partial t$ is replaced by $\partial/\partial t + \boldsymbol{U}(t)\cdot\nabla$ in the governing equations (2.2). It is convenient to work in the frame moving with the tidal flow $\boldsymbol{U}(t)$ (see Bell 1975*a*, and Khatiwala 2003 for details).

We are interested in overturning of the stratification surfaces, i.e. where and when $\partial\Theta/\partial z$ is negative. For finite tidal excursion, (2.23) becomes

$$\frac{\partial\Theta}{\partial z} = N^2\left\{1 - \sum_{n=1}^{n_0} \mathrm{Re}\left[e^{-in\omega_0 t} A_n\left(x - \frac{U_0}{\omega_0}\sin\omega_0 t, z\right)\right]\right\} \tag{B 1}$$

where $A_n(x, z) = G_n(x, z) * A_n(x, 0)$, $\hat{G}_n(k, z) = e^{-i|k|\mu_n z}$

$$\hat{A}_n(k, 0) = i|k|(-1)^{n+1}\mu_n\hat{h}(k)2J_n\left(\frac{U_0 k}{\omega_0}\right)$$

where $\mu_n = \sqrt{(N^2 - n^2\omega_0^2)/(n^2\omega_0^2 - f^2)}$ and $J_n(x)$ is the Bessel function of the first kind of order n. In the above equations, we only kept the oscillating contribution to the solution, i.e. modes with $n \leqslant n_0$, where n_0 is the largest integer strictly smaller than N/ω_0. Equation (B 1) has two interesting consequences. First, each mode n has characteristics with slope μ_n^{-1}. Hence different modes will generate instabilities near characteristics with different slopes, and for isolated topography we can study the instability of each mode separately. Secondly, the vertical propagation for each mode is still governed by convolution with a Green's function $G_n(x, z) = G(x, \mu_n z)$, where $G(x, Z)$ is given in (2.17).

We can write the bottom amplitude $A_n(x,0)$ in real-space coordinates using the identity (e.g. Bell 1975*a*)

$$FT^{-1}\{2J_n(k)/k^n\} = g_n(x) \equiv \frac{(1-x^2)^{n-1/2}\chi_{|x|<1}}{\sqrt{\pi}\,\Gamma(n+1/2)2^{n-1}}. \tag{B 2}$$

This yields

$$A_n(x,0) = \mathrm{i}^{n-1}\mu_n \left(\frac{U_0}{\omega_0}\right)^{n-1} \tilde{f}_n(x) \text{ where } f_n(x) = \frac{\mathrm{d}^{n+1}h}{\mathrm{d}x^{n+1}} * g_n\left(\frac{x}{U_0/\omega_0}\right). \tag{B 3}$$

Specifically, the amplitude for the fundamental mode is

$$A_1(x,z) = G_1(x,z) * A_1(x,0),\ A_1(x,0) = \mu_1 \tilde{f}_1(x) \text{ where } f_1(x) = \frac{\mathrm{d}^2 h}{\mathrm{d}x^2} * g_1\left(\frac{x}{U_0/\omega_0}\right).$$

By allowing for finite excursion, we find that the amplitude of the fundamental mode is proportional to the Hilbert transform of h'' convoluted with the compactly supported function $g_1(x\omega_0/U_0)$. Hence integrable singularities in $\tilde{h}''$ will be smoothed by convolution with this compactly supported function. In the case of jumps in h'' and logarithmic singularities of $\tilde{h}''$ discussed in § 2.3, this now yields an increased but finite wave amplitude at the jump locations. For small excursion $kU_0/\omega_0 \ll 1$, $J_n(kU_0/\omega_0) \approx (kU_0/2\omega_0)^n/n!$, $g_1(x\omega_0/U_0) \to \delta(x)U_0/\omega_0$, the fundamental frequency response dominates the wave field and we can recover the solution of the small excursion regime from (B 1).

B.2. *Three-dimensional flow over two-dimensional topography*

We now turn to the three-dimensional problem and compute the amplitude of the wave field for finite tidal excursion. We use the same notation as in § 3. In particular, the horizontal coordinates and wavenumbers are respectively denoted $\boldsymbol{x} = (x, y)$ and $\boldsymbol{k} = (k, l)$, and we denote $|\boldsymbol{k}| = \kappa$. As in § B.1 we compute the perturbation of the stratification due to the waves and (3.22) becomes

$$\frac{\partial \Theta}{\partial z} = N^2 \left\{1 - \sum_{n=1}^{n_0} \mathrm{Re}\left[\mathrm{e}^{-\mathrm{i}n\omega_0 t} A_n\left(x - \frac{U_0}{\omega_0}\sin\omega_0 t,\, y,\, z\right)\right]\right\} \tag{B 4}$$

with

$$A_n(\boldsymbol{x},z) = G_n(\boldsymbol{x},z) * A_n(\boldsymbol{x},0),\ \hat{G}_n(\boldsymbol{k},z) = \mathrm{e}^{-\mathrm{i}\kappa\mu_n z}$$
$$\hat{A}_n(\boldsymbol{k},0) = \mathrm{i}\kappa(-1)^{n+1}\mu_n \hat{h}(\boldsymbol{k}) 2J_n\left(\frac{U_0 k}{\omega_0}\right)$$

where $\mu_n = \sqrt{(N^2 - n^2\omega_0^2)/(n^2\omega_0^2 - f^2)}$, $J_n(x)$ is the Bessel function of the first kind of order n and n_0 is the largest integer strictly smaller than N/ω_0. We see that each mode has a front near a forward cone with slope μ_n^{-1}. Hence different modes will lead to instabilities near different cones, and for isolated topography we can study the instability of each mode separately. The vertical propagation of each mode is still governed by a propagator $G_n(\boldsymbol{x},z) = G(\boldsymbol{x},\mu_n z)$, where $G(\boldsymbol{x},Z)$ is given by (3.18).

The bottom amplitude $A_n(\boldsymbol{x},0)$ can be computed in real-space coordinates

$$A_n(\boldsymbol{x},0) = \mathrm{i}^{n-1}\mu_n \left(\frac{U_0}{\omega_0}\right)^{n-1} \sqrt{-\Delta}\left\{\frac{\partial^n h}{\partial x^n}(x,y) *_x g_n\left(\frac{x}{U_0/\omega_0}\right)\right\}, \tag{B 5}$$

where $g_n(x)$ is given by (B 2) and $*_x$ denotes convolution with respect to the variable x only. As in § B.1, we can recover the small excursion solution if $kU_0/\omega_0 \ll 1$.

Appendix C. Asymptotic behaviour of the amplitude for the Gaussian boundary amplitude

C.1. *Asymptotic behaviour of* $Re(f(\bar{Z},\bar{Z}))$

From (4.5), we want the asymptotic behaviour of

$$\mathrm{Re}(f(\bar{Z},\bar{Z})=\frac{1}{2\pi}\int_0^1\int_{-\pi}^{\pi}\frac{\mathrm{e}^{-\bar{Z}^2(1+u^2-2u\cos\theta)/2}}{\sqrt{1-u^2}}(1+\bar{Z}^2u(\cos\theta-u))\,\mathrm{d}\theta\,u\,\mathrm{d}u \tag{C 1}$$

as $\bar{Z}\to\infty$. We apply Laplace's method to the first part of the above integral:

$$\begin{aligned}\int_0^1\int_{-\pi}^{\pi}\frac{\mathrm{e}^{-\bar{Z}^2(1+u^2-2u\cos\theta)/2}}{\sqrt{1-u^2}}\,\mathrm{d}\theta\,u\,\mathrm{d}u\;&\approx\int_0^1\frac{u\mathrm{e}^{-\bar{Z}^2(1+u^2)/2}}{\sqrt{1-u^2}}\int_{-\epsilon}^{\epsilon}\mathrm{e}^{\bar{Z}^2u(1-\theta^2/2)}\,\mathrm{d}\theta\,\mathrm{d}u\\
&\approx\int_0^1\frac{u\mathrm{e}^{-\bar{Z}^2(1-u)^2/2}}{\sqrt{1-u^2}}\int_{-\infty}^{\infty}\mathrm{e}^{-\bar{Z}^2u\theta^2/2}\,\mathrm{d}\theta\,\mathrm{d}u\;\approx\frac{\sqrt{2\pi}}{\bar{Z}}\int_0^1\frac{\sqrt{u}\mathrm{e}^{-\bar{Z}^2(1-u)^2/2}}{\sqrt{1-u^2}}\,\mathrm{d}u\\
&\approx\frac{\sqrt{2\pi}}{\bar{Z}}\int_0^{\epsilon}\frac{\sqrt{1-u}}{\sqrt{u}\sqrt{2-u}}\mathrm{e}^{-\bar{Z}^2u^2/2}\,\mathrm{d}u\approx\frac{\sqrt{\pi}}{\bar{Z}}\int_0^{\epsilon}\frac{\mathrm{e}^{-\bar{Z}^2u^2/2}}{\sqrt{u}}\,\mathrm{d}u\\
&\approx\frac{\sqrt{\pi}}{\bar{Z}}\int_0^{\infty}\frac{\mathrm{e}^{-s}}{2^{3/4}s^{3/4}\sqrt{\bar{Z}}}\,\mathrm{d}s\approx\frac{\sqrt{\pi}\;\Gamma(1/4)}{\bar{Z}^{3/2}\;2^{3/4}},\end{aligned} \tag{C 2}$$

where Γ denotes the gamma function $\Gamma(z)=\int_0^{\infty}u^{z-1}\mathrm{e}^{-u}\,\mathrm{d}u$.

Similarly

$$\int_0^1\int_{-\pi}^{\pi}\frac{\mathrm{e}^{-\bar{Z}^2(1+u^2-2u\cos\theta)/2}}{\sqrt{1-u^2}}u(\cos\theta-u)\,\mathrm{d}\theta\,u\,\mathrm{d}u$$

$$\approx\int_0^1\frac{u^2\mathrm{e}^{-\bar{Z}^2(1+u^2)/2}}{\sqrt{1-u^2}}\int_{-\epsilon}^{\epsilon}\mathrm{e}^{\bar{Z}^2u(1-\theta^2/2)}(1-u)\,\mathrm{d}\theta\,\mathrm{d}u \tag{C 3}$$

$$\approx\int_0^1\frac{u^2(1-u)\mathrm{e}^{-\bar{Z}^2(1-u)^2/2}}{\sqrt{1-u^2}}\int_{-\infty}^{\infty}\mathrm{e}^{-\bar{Z}^2u\theta^2/2}\,\mathrm{d}\theta\,\mathrm{d}u$$

$$\approx\frac{\sqrt{2\pi}}{\bar{Z}}\int_0^1\frac{u^{3/2}\sqrt{1-u}\mathrm{e}^{-\bar{Z}^2(1-u)^2/2}}{\sqrt{1+u}}\,\mathrm{d}u \tag{C 4}$$

$$\approx\frac{\sqrt{2\pi}}{\bar{Z}}\int_0^{\epsilon}\frac{(1-u)^{3/2}\sqrt{u}}{\sqrt{2-u}}\mathrm{e}^{-\bar{Z}^2u^2/2}\,\mathrm{d}u\approx\frac{\sqrt{\pi}}{\bar{Z}}\int_0^{\epsilon}\mathrm{e}^{-\bar{Z}^2u^2/2}\sqrt{u}\,\mathrm{d}u$$

$$\approx\frac{\sqrt{\pi}}{\bar{Z}}\int_0^{\infty}\mathrm{e}^{-s}s^{-1/4}2^{-1/4}\bar{Z}^{-3/2}\,\mathrm{d}s\approx\frac{\sqrt{\pi}\;\Gamma(3/4)}{\bar{Z}^{5/2}\;2^{1/4}}. \tag{C 5}$$

Since

$$\frac{\sqrt{\pi}\;\Gamma(1/4)}{\bar{Z}^{3/2}\;2^{3/4}}\ll\bar{Z}^2\frac{\sqrt{\pi}\;\Gamma(3/4)}{\bar{Z}^{5/2}\;2^{1/4}}, \tag{C 6}$$

we obtain

$$\mathrm{Re}(f(\bar{Z},\bar{Z}))\approx\frac{2^{-5/4}\pi^{-1/2}\;\Gamma(3/4)}{\bar{Z}^{1/2}}\;\text{ as }\bar{Z}\to\infty. \tag{C 7}$$

C.2. *Asymptotic behaviour of* $Im(f(\bar{Z},\bar{Z}))$

Using (4.5) and the same method as in § C.1, we find

$$\mathrm{Im}(f(\bar{Z},\bar{Z}))\approx-\frac{2^{-5/4}\pi^{-1/2}\;\Gamma(3/4)}{\bar{Z}^{1/2}}\;\text{ as }\bar{Z}\to\infty. \tag{C 8}$$

REFERENCES

Alford, M. H., Gregg, M. C. & Merrifield, M. A. 2006 Structure, propagatio and mixing of energetic baroclinic tides in Mamala Bay, Oahu, Hawaii. *J. Phys. Oceanogr.* **36**, 997–1018.

Aucan, J., Merrifield, M. A., Luther, D. S. & Flament, P. 2006 Tidal mixing events on the deep flanks of Kaena Ridge, Hawaii. *J. Phys. Oceanogr.* **36**, 1202–1219.

Baines, P. G. 1973 The generation of internal tides by flat-bump topography. *Deep-Sea Res.* **20**, 179–205.

Balmforth, N. J., Ierley, G. R. & Young, W. R. 2002 Tidal conversion by subcritical topography. *J. Phys. Oceanogr.* **32**, 2900–2914.

Bell, T. H. 1975*a* Lee waves in stratified flows with simple harmonic time dependence. *J. Fluid Mech.* **67**, 705–722.

Bell, T. H. 1975*b* Topographically generated internal waves in the open ocean. *J. Geophys. Res.* **80**, 320–327.

Bender, C. M. & Orszag, S. A. 2005 Asymptotic expansion of integrals. In *Advanced Mathematical Methods for Scientists and Engineers*, 1st edn, pp. 247–316. Springer.

Canuto, V. M., Howard, A. M., Muller, C. J. & Jayne, S. R. 2007 Giss mixing model: Inclusion of tides and bottom boundary layer. *Ocean Modelling* (submitted).

Cox, C. & Sandstrom, H. 1962 Coupling of internal and surface waves in water of variable depth. *J. Oceanogr. Soc. Japan* **18**, 499–513.

Di Lorenzo, E., Young, W. R. & Llewellyn Smith, S. G. 2006 Numerical and analytical estimates of M 2 tidal conversion at steep oceanic ridges. *J. Phys. Oceanogr.* **36**, 1072–1084.

Egbert, G. D. & Ray, R. D. 2000 Significant dissipation of tidal energy in the deep ocean inferred from satellite altimeter data. *Nature* **405**, 775–778.

Egbert, G. D. & Ray, R. D. 2001 Estimates of M2 tidal energy dissipation from TOPEX/Poseidon altimeter data. *J. Geophys. Res.* **106**, 22475–22502.

Evans, L. C. 1998 Convolution and smoothing. In *Partial Differential Equations*, *Graduate Studies in Mathematics*, vol. 19, pp. 629–631. AMS.

Garrett, C. & Kunze, E. 2007 Internal tide generation in the deep ocean. *Annu. Rev. Fluid Mech.* **39**, 57–87.

Hibiya, T., Nagasawa, M. & Niwa, Y. 2006 Global mapping of diapycnal diffusivity in the deep ocean based on the results of expendable current profiler (XCP) surveys. *Geophys. Res. Lett.* **33** (3).

Jayne, S. R. & Laurent, L. C. S. 2001 Parameterizing tidal dissipation over rough topography. *Geophys. Res. Lett.* **28**, 811–814.

Khatiwala, S. 2003 Generation of internal tides in an ocean of finite depth: Analytical and numerical calculations. *Deep-Sea Res.* **50**, 3–21.

Klymak, J. M., Moum, J. N., Nash, J. D., Kunze, E., Girton, J. B., Carter, G. S., Lee, C. M., Sanford, T. B. & Gregg, M. C. 2006 An estimate of tidal energy lost to turbulence at the Hawaiian Ridge. *J. Phys. Oceanogr.* **36**, 1148–1164.

Ledwell, J. R., Montgomery, E. T., Polzin, K. L., St Laurent, L. C., Schmitt, R. W. & Toole, J. M. 2000 Evidence for enhanced mixing over rough topography in the abyssal ocean. *Nature* **403**, 179–82.

Lee, C. M., Kunze, E., Sanford, T. B., Nash, J. D., Merrifield, M. A. & Holloway, P. E. 2006 Internal tides and turbulence along the 3000-m isobath of the Hawaiian Ridge with model comparisons. *J. Phys. Oceanogr.* **36**, 1165–1183.

Legg, S. & Huijts, K. M. H. 2006 Preliminary simulations of internal waves and mixing generated by finite amplitude tidal flow over isolated topography. *Deep-Sea Res. II* **53**, 140–156.

Llewellyn Smith, S. G. & Young, W. R. 2002 Conversion of the barotropic tide. *J. Phys. Oceanogr.* **32**, 1554–1566.

Llewellyn Smith, S. G. & Young, W. R. 2003 Tidal conversion at a very steep ridge. *J. Fluid Mech.* **495**, 175–191.

Maas, L. R. M. & Lam, F. P. A. 1995 Geometric focusing of internal waves. *J. Fluid Mech.* **300**, 1–41.

Munk, W. & Wunsch, C. 1998 Abyssal recipes II: Energetics of tidal and wind mixing. *Deep-Sea Res. Part I: Oceanogr. Res. Papers* **45**, 1977–2010.

Nycander, J. 2005 Generation of internal waves in the deep ocean by tides. *J. Geophys. Res.* **110**.

Petrelis, F., Llewellyn Smith, S. G. & Young, W. R. 2006 Tidal conversion at a submarine ridge. *J. Phys. Oceanogr.* **36**, 1053–1071.

Polzin, K. L., Toole, J. M., Ledwell, J. R. & Schmitt, R. W. 1997 Spatial variability of turbulent mixing in the abyssal ocean. *Science* **276**, 93–96.

Robinson, R. M. 1969 The effect of a vertical barrier on internal waves. *Deep-Sea Res.* **16**, 421–429.

Saenko, O. A. & Merryfield, W. J. 2005 On the effect of topographically enhanced mixing on the global ocean circulation. *J. Phys. Oceanogr.* **35**, 826–834.

Seibold, E. & Berger, W. H. 1996 *The Sea Floor: An Introduction to Marine Geology*. Springer.

Simmons, H. L., Jayne, S. R., St. Laurent, L. C. & Weaver, A. J. 2004 Tidally driven mixing in a numerical model of the ocean general circulation. *Ocean Modelling* **6**, 245–263.

Smith, W. H. F. & Sandwell, D. T. 1997 Global sea floor topography from satellite altimetry and ship depth soundings. *Science* **277**, 1956–1962.

Sobolev, S. L. 1960 On the motion of a symmetric top with a cavity filled by a fluid. *J. Appl. Mech. Tech. Phys.* **3**, 20–55.

St. Laurent, L. C. & Garrett, C. 2002 The role of internal tides in mixing the deep ocean. *J. Phys. Oceanogr.* **32**, 2882–2899.

St. Laurent, L. C., Simmons, H. L. & Jayne, S. R. 2002 Estimating tidally driven mixing in the deep ocean. *Geophys. Res. Lett.* **29**, 2106.

St. Laurent, L. C., Stringer, S., Garrett, C. & Perrault-Joncas, D. 2003 The generation of internal tides at abrupt topography. *Deep-Sea Res. I* **50**, 987–1003.

Stein, E. M. 1970 Differentiability properties in terms of function spaces. In *Singular Integrals and Differentiability Properties of Functions*, pp. 116–165. Princeton University Press.

Thorpe, S. A. 2005 *The Turbulent Ocean*. Cambridge University Press.

Watson, G. N. 1966 In *A Treatise on the Theory of Bessel Functions*, 2nd edn, p. 405. Cambridge University Press.

Wunsch, C. 2000 Moon, tides and climate. *Nature* **405**, 743–4.

Wunsch, C. & Ferrari, R. 2004 Vertical mixing, energy, and the general circulation of the oceans. *Annu. Rev. Fluid Mech.* **36**, 281–314.